

Shaping Dark Photon Spectral Distortions

Giorgi Arsenadze,^{1,*} Andrea Caputo,^{2,†} Xucheng Gan,^{1,3,‡} Hongwan Liu,^{4,5,6,§} and Joshua T. Ruderman^{1,¶}¹*Center for Cosmology and Particle Physics, Department of Physics,
New York University, New York, NY 10003, USA*²*Theoretical Physics Department, CERN, 1211 Geneva 23, Switzerland*³*Deutsches Elektronen-Synchrotron DESY, Notkestr. 85, 22607 Hamburg, Germany*⁴*Physics Department, Boston University, Boston, MA 02215, USA*⁵*Kavli Institute for Cosmological Physics, University of Chicago, Chicago, IL 60637*⁶*Theoretical Physics Department, Fermi National Accelerator Laboratory, Batavia, IL 60510*

The cosmic microwave background (CMB) spectrum is an extraordinary tool for exploring physics beyond the Standard Model. The exquisite precision of the measurement makes it particularly sensitive to small effects caused by hidden sector interactions. In particular, CMB spectral distortions can unveil the existence of dark photons which are kinetically coupled to the standard photon. In this work, we use the COBE-FIRAS dataset to derive accurate and robust limits on photon-to-dark-photon oscillations for a large range of dark photon masses, from 10^{-10} to 10^{-4} eV. We consider in detail the redshift dependence of the bounds, computing CMB distortions due to photon injection/removal using a Green's function method. Our treatment improves on previous results, which had set limits studying energy injection/removal into baryons rather than photon injection/removal, or ignored the redshift evolution of distortions. The difference between our treatment and previous ones is particularly noticeable in the predicted spectral shape of the distortions, a smoking gun signature for photon-to-dark-photon oscillations. The characterization of the spectral shape is crucial for future CMB missions, which could improve the present sensitivity by orders of magnitude, exploring regions of the dark photon parameter space that are otherwise difficult to access. 

arXiv:2409.12940v1 [astro-ph.CO] 19 Sep 2024

* ga1348@nyu.edu

† andrea.caputo@cern.ch

‡ xg767@nyu.edu; xucheng.gan@desy.de

§ hongwan@bu.edu

¶ ruderman@nyu.edu

CONTENTS

I. Introduction	2
II. Photon-To-Dark-Photon Oscillations	4
III. Spectral Distortions	6
IV. Green's Function Method	9
V. Spectral Distortion from $\gamma \rightarrow A'$ and COBE-FIRAS Constraints	12
VI. Conclusions	18
A. Profile Likelihood Test	19
B. Constants	19
C. Monochromatic Photon Injection in the μ -Era	20
D. Green's Functions	21
1. Functions	22
2. Green's Function Normalization	22
3. Green's Function in the μ -Era	23
4. Green's Function in the y -Era	23
5. Green's Function for Pure Energy Injection	24
References	25

I. INTRODUCTION

The dark photon A' is a hypothetical particle that can open one of only a few renormalizable portals between the Standard Model (SM) sector and the dark sector. A significant research program is ongoing to detect dark photons with a mass of $m_{A'} \lesssim 10^{-3}$ eV. The dark photon parameter space can be tested by terrestrial experiments, such as the Cavendish-Coulomb experiments [1–4], Light-Shining-Through-Walls experiments [5–10], helioscopes [11–14], and the direct detection of dark photons produced in the Sun [15–18]. The dark photon parameter space can also be tested through astrophysical probes such as stellar energy loss [11, 19–26] and black hole superradiance [27–30]. Moreover, because the dark photon can impact the SM electromagnetic field through the kinetic mixing portal, the magnetosphere of Jupiter [31–33] and Earth [3, 32, 34–36] can also be used to constrain the kinetic mixing parameter of ultralight dark photons in the 10^{-16} eV— 10^{-13} eV mass range. For a complete review of the dark photon limits, one can refer to Ref. [37]. All dark photon searches are, however, limited by the decoupling of all interactions with the SM when the dark photon mass vanishes, $m_{A'} \rightarrow 0$, which makes detection increasingly difficult at low masses [15, 22, 38].

Compared with the aforementioned detection methods, distortions to the blackbody spectrum of the cosmic microwave background (CMB) serves as one of the most sensitive ways to explore the dark photon parameter space for $m_{A'} \lesssim 10^{-4}$ eV [39–48]. In the early universe, CMB photons were in chemical equilibrium with baryons, and their phase space density obeyed the blackbody distribution with zero chemical potential. Within standard Λ CDM cosmology, this blackbody distribution should be mostly preserved through the process of recombination until the present day. The COBE-FIRAS measurement of this spectrum confirmed this prediction, finding that any deviation of the CMB phase space from a blackbody distribution has to be less than 1 part in 10^4 [49]. Any exotic process that injects energy into the CMB after the CMB photons fall out of chemical equilibrium potentially imprints a distortion away from the blackbody spectrum. Precise measurements of the CMB spectrum are therefore a powerful tool for detecting not just dark photons, but also axions [40, 50–53], dark matter decay/annihilation/scattering [54], and inflation [55].

Significant spectral distortions caused by dark photons can arise if photons γ and A' kinetically mix, resulting in a sufficiently large probability of $\gamma \rightarrow A'$ conversions throughout cosmic history, removing photons from the CMB blackbody spectrum. The conversion probability of CMB photons into dark photons is dominated by resonant conversions between the two states, which occur whenever the effective plasma mass of the SM photon γ —induced mainly by the density of free electrons—matches $m_{A'}$, the dark photon mass [39, 42–44, 56, 57].

The impact of $\gamma \rightarrow A'$ on the CMB spectrum can be classified into two broad regimes: $m_{A'} \lesssim 10^{-9}$ eV, and $m_{A'} \gtrsim 10^{-9}$ eV. For $m_{A'} \lesssim 10^{-9}$ eV, resonant conversions only occur after recombination when photons are free-streaming; the distorted spectrum produced as a result of $\gamma \rightarrow A'$ evolves only through redshifting as a function of time after the conversion has occurred. This regime was first studied in Ref. [39], and extended to include the effect of inhomogeneities on resonance conversion by Ref. [43, 44] (see also Ref. [58]). The signal from the inverse process, $A' \rightarrow \gamma$, for dark photon dark matter have been discussed in Refs. [42–44, 59–66]. Throughout the rest of the paper, we assume that there is no initial abundance of the dark photon, and consider only the $\gamma \rightarrow A'$ process.

More recently, Refs. [46–48] have examined the impact of $\gamma \rightarrow A'$ on the CMB anisotropy power spectrum. These results rely on the fact that $\gamma \rightarrow A'$ resonant conversion is highly sensitive to the free electron number density, and is therefore correlated with cosmic structures, leading to nontrivial spatial correlations. These works have demonstrated impressive limits for $m_{A'} \lesssim 10^{-9}$ eV, when $\gamma \rightarrow A'$ occurs after recombination.

In this paper, we instead focus on the regime $m_{A'} \gtrsim 10^{-9}$ eV, when resonant conversions happen before recombination. At such high redshifts, inhomogeneities are unimportant, and we can safely take the universe to be homogeneous [44]. Our goal is to accurately compute the spectral distortion produced by these conversions, and use the COBE-FIRAS data to set limits on ϵ as a function of $m_{A'}$. This regime was first considered in Ref. [39]; however, they assumed that the spectral distortion produced by resonant conversion only evolved via redshifting, *i.e.* that photons are always free-streaming. In fact, any spectral distortion can potentially be redistributed as a function of time due to highly efficient Compton scattering between photons and electrons in the epoch before recombination. Subsequently, Ref. [42] derived limits on ϵ by assuming that distortions from $\gamma \rightarrow A'$ conversions are identical to distortions produced in the CMB when the equivalent amount of energy is removed from baryons at the same redshift, leading to so-called pure μ - and y -distortions. This, however, is also not a good approximation: the actual CMB spectral distortion from photon removal can be significantly different from those corresponding to energy removal from baryons, as pointed out in Ref. [67]. The spectral distortion therefore does not correspond to a pure μ - or y -distortion, and cannot be compared directly to limits on the $|\mu|$ and $|y|$ parameters, as was done in Ref. [42]. Instead, the full distortion must be carefully computed, and compared to the full COBE-FIRAS data.

We apply the Green’s function method developed in Ref. [67] for photon injection/removal to accurately compute the spectral distortion due to $\gamma \rightarrow A'$ conversions. We obtain accurate results when resonant conversions occur during the μ -era (when Compton scattering is highly efficient at redistributing photons, applicable to $m_{A'}$ in the approximate range of 3×10^{-6} eV— 5×10^{-5} eV) and in the y -era (when Compton scattering is inefficient, applicable to $m_{A'}$ in the approximate range of 10^{-9} eV— 2×10^{-8} eV). In the intermediate μ - y transition era, we have obtained reliable approximations for the spectral distortion, allowing us to set a conservative limit on ϵ in the mass range 2×10^{-8} eV— 3×10^{-6} eV. Our new limits strengthen existing limits by up to a factor of 3, and are particularly important in setting a benchmark for upcoming Light-Shining-Through-Walls experiments such as DarkSRF, which offer a complementary search strategy for dark photons in the 10^{-9} eV— 10^{-5} eV range [68]. Some of our new results have been already presented elsewhere by several of us [69, 70]; here we provide the complete analysis.

The rest of this paper is organized as follows. In Sec. II, we introduce the dark photon model and give a back-of-the-envelope estimation of its COBE-FIRAS constraints. In Sec. III, we discuss the different stages of the early universe as classified by the efficiency of Compton scattering (CS), bremsstrahlung (BR), and double Compton scattering (DCS). We also describe some important concepts in spectral distortions. In Sec. IV, we introduce the Green’s function method and explain how the spectral distortion, in the case of $\gamma \rightarrow A'$ conversions, is calculated. In Sec. V, we present our main result: the COBE-FIRAS spectral distortion limits on ϵ as a function of $m_{A'}$. We compare our updated COBE-FIRAS constraint using the complete treatment with previous results. We also examine the CMB spectral distortion signal from $\gamma \rightarrow A'$ in detail at different representative points in the dark photon parameter space. We discuss the impact of an important approximation made in deriving our limits over a small range in $m_{A'}$. Details of our data analysis method, the complete table of the constants appearing in the CMB spectral distortion calculation, the derivation of the μ distortion for the simplified monochromatic photon

injection/removal, and the detailed discussion of Green's functions in different eras can be found in Appendix A, Appendix B, Appendix C, Appendix D, respectively. We use $\hbar = c = k_B = 1$ for expressions given in this paper but will use radio astronomy units in plots where appropriate. The code for obtaining our results are publicly available at <https://github.com/GiorgiArsenadze/Shaping-Dark-Photon-Spectral-Distortions> .

II. PHOTON-TO-DARK-PHOTON OSCILLATIONS

In this section, we give a brief introduction to $\gamma \rightarrow A'$ conversions. We begin with the low-energy Lagrangian describing this model,

$$\mathcal{L} = -\frac{1}{4}F_{\mu\nu}F^{\mu\nu} - \frac{1}{4}F'_{\mu\nu}F'^{\mu\nu} + \frac{\epsilon}{2}F_{\mu\nu}F'^{\mu\nu} - \frac{1}{2}m_{A'}^2 A'_\mu A'^\mu + eA_\mu j_e^\mu, \quad (1)$$

where $A^{(\prime)}$ is the field of the photon (dark photon), and $F^{(\prime)}$ is the corresponding field strength. Here, e is the gauge coupling of the electromagnetic $U(1)$ gauge field, j_e is the electromagnetic current, and the dimensionless quantity ϵ parameterizes the size of kinetic mixing between the photon and the dark photon. Here, ϵ obeys the upper bound $\epsilon < 1$ according to the requirement of the positive-definiteness of the gauge kinetic terms [71, 72]; a small value of ϵ is technically natural, and can be realized in several ultraviolet completions of such a model [73, 74]. In our work, we investigate the minimal scenario of the kinetic mixing portal, where only the dark photon is in the dark sector, with a negligible initial abundance. If there are additional particles charged under an ultralight dark photon that mixes with the SM photon, these particles would appear to be millicharged and can drastically alter the expected signal. Such modifications include an irreducible cosmic millicharge background [75, 76], a millicharged-particle-induced dark plasma mass [77, 78], and dark thermalization inside stars [79, 80].

Because the photon is coupled with the electron current, in the finite density environment of the early universe, the electrons induce an effective plasma mass [81] given by

$$\begin{aligned} m_\gamma^2(z) &= \frac{e^2 n_e(z)}{m_e} - \omega^2(z) (\mathbf{n}_{\text{HI}}^2(z) - 1) \\ &\simeq 1.4 \times 10^{-21} \text{eV}^2 \left(\frac{n_e(z)}{\text{cm}^{-3}} \right) - 8.4 \times 10^{-24} \text{eV}^2 \left(\frac{\omega(z)}{\text{eV}} \right)^2 \left(\frac{n_{\text{HI}}(z)}{\text{cm}^{-3}} \right), \end{aligned} \quad (2)$$

where \mathbf{n}_{HI} is the refractive index of neutral hydrogen, n_{HI} is the number density of neutral hydrogen, and n_e is the free electron number density. We obtain n_e and n_{HI} from CLASS, which uses HyRec to model recombination [82, 83], and uses the tanh scenario for the reionization [84].¹ We adopt cosmological parameters consistent with Planck 2018 [84]. Eq. (2) represents the modification of the dispersion relation in the presence of an optically dense medium. Here, the positive term comes from the free electrons, and the negative term comes from neutral hydrogen [77]. The present work mainly focuses on dark photon phenomenology at high redshifts, above $z \sim 100$, where baryon fluctuations are negligible and the universe can be considered homogeneous. In Fig. 1, we illustrate the cosmological evolution of the photon plasma mass as a function of the redshift. Based on the efficiencies of various processes which control the evolution of spectral distortions, we can divide the universe into five distinct eras: free-streaming era (purple), y -era (blue), μ - y transition era (green), μ -era (orange), and T -era (red); these different eras will be described in detail in Sec. III. We plot the plasma frequency evolution for two different values of the photon energy ω , which enters the second term in Eq. 2. To characterise the photon energy, we introduce the redshift-independent quantity $x \equiv \omega_0/T_0$, with ω_0 and T_0 being the present-day CMB photon energy and temperature, respectively. We show the plasma frequency evolution for $x = 1$ and $x = 5$. The plasma mass for $x = 5$ becomes negative during $200 \lesssim z \lesssim 900$, due to the negative mass squared contribution from neutral hydrogen after hydrogen recombination. However, our focus will be on the period well before hydrogen recombination, when the contribution from neutral hydrogen is negligible and thus the plasma frequency evolution is identical for both $x = 1$ and $x = 5$.

¹ The choice of modeling for reionization is not important for this paper, since we are only concerned with high-redshift conversions.

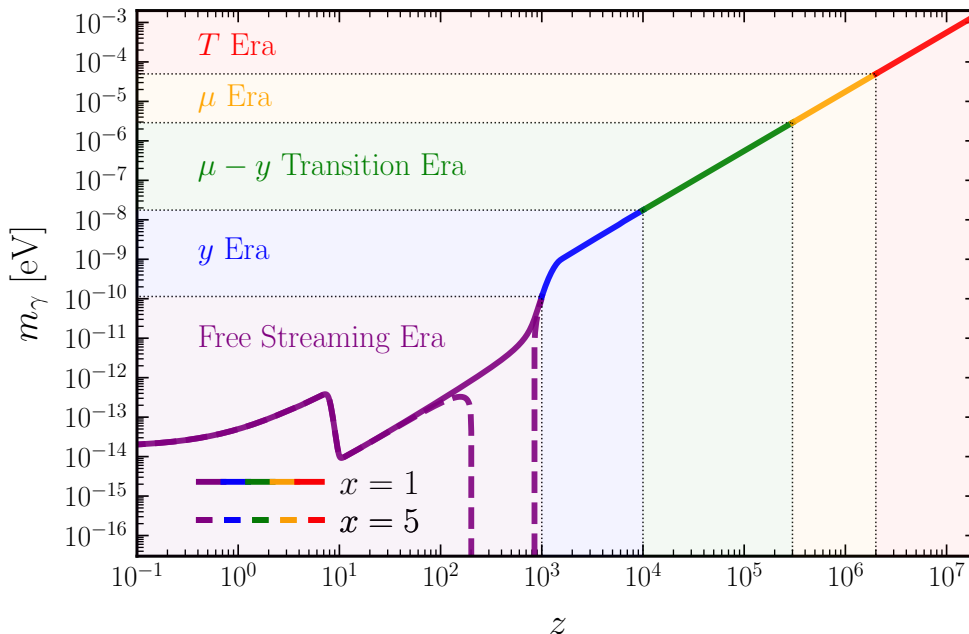


FIG. 1. The cosmological evolution of the photon’s effective plasma mass as a function of the redshift. Based on the efficiency of the scattering channels discussed in Sec. III, the universe can be divided into five eras: the free streaming era (purple), y -era (blue), μ - y transition era (green), μ -era (orange), and T era (red). Here, we show the evolution for two different photon energies, $x = 1$ and $x = 5$, which are the solid and dashed lines, respectively. The $x = 5$ line dips down in the period $2 \times 10^2 < z < 9 \times 10^2$, due to the negative mass squared contribution from the neutral Hydrogen. In other periods, when most of the neutral Hydrogen is ionized, the difference between $x = 5$ and $x = 1$ is very small.

The effective plasma mass, $m_\gamma^2(z)$, evolves throughout the expansion of the universe, and it may match $m_{A'}^2$ at some point during the cosmological history. If this happens, then a resonant $\gamma \rightarrow A'$ conversion can take place. These conversions can be modeled as a Landau-Zener transition [56, 57], and has been extensively explored in the context of neutrino oscillation [85, 86], and dark photons [6, 39, 43, 44, 87]. The rate for the $\gamma \rightarrow A'$ transition reads [43, 44, 77]

$$\Gamma_{\gamma \rightarrow A'}(z) = \frac{\epsilon^2 m_{A'}^4 \Gamma_\gamma}{(m_\gamma^2(z) - m_{A'}^2)^2 + \omega^2(z) \Gamma_\gamma^2}, \quad (3)$$

where Γ_γ is the damping rate of the plasmon quanta. Under the narrow width approximation $\Gamma_\gamma \ll m_{A'}^2/\omega$, the associated conversion probability can be written as

$$P_{\gamma \rightarrow A'}(\omega) = \int dt \Gamma_{\gamma \rightarrow A'} = \frac{\pi \epsilon^2 m_\gamma^2(z_{\text{res}})}{\omega(z_{\text{res}})(1 + z_{\text{res}})H(z_{\text{res}})} \left| \frac{d \log m_\gamma^2}{dz} \right|_{\text{res}}^{-1}, \quad (4)$$

where “res” labels the time when $m_\gamma^2 = m_{A'}^2$, $\omega(z_{\text{res}}) = \omega_0(1 + z_{\text{res}})$, and $dt = -dz/(1 + z)H(z)$, with $H(z)$ being the Hubble parameter.

We note here that rapid scattering of γ with free electrons in the plasma can affect the process of resonant conversion. In order for scattering to have a negligible effect, the resonance timescale, τ_r (the inverse of the resonant width), must be significantly smaller than the Compton scattering timescale (or, equivalently, the mean free path) τ_s for photons in the plasma. For the masses and kinetic mixing of interest in this work, we have checked that $\tau_r \ll \tau_s$.

In order to provide some intuition for typical values and mass scaling of the conversion probability, let us briefly focus on dark photon masses $m_{A'} \gtrsim 10^{-9}\text{eV}$ and work out some simple estimates. In this case, the $\gamma \rightarrow A'$ transition happens in the radiation-dominated (RAD) era. At this time, hydrogen atoms are fully ionized, which gives $m_\gamma^2(z) \propto$

$n_e(z) \propto (1+z)^3$. Using the fact that $H(z) = H_0 \Omega_r^{1/2} (1+z)^2$ for the RAD era, where H_0 is the Hubble constant, $\Omega_r = \Omega_m / (1+z_{\text{eq}})$, z_{eq} is the redshift of matter-radiation equality, and Ω_m is the matter density parameter, we get

$$\text{RAD: } P_{\gamma \rightarrow A'}(x) \simeq \frac{\epsilon^2 \mathcal{F}}{x} \quad \text{with} \quad \mathcal{F} = \frac{\pi m_\gamma^2(z=0)}{3 \Omega_r^{1/2} H_0 T_0} \simeq 10^{11}. \quad (5)$$

To calculate the numerical value of \mathcal{F} , we used $m_\gamma(z=0) \simeq 1.7 \times 10^{-14}$ eV. The first thing we notice in Eq. (5) is that any dependence on $m_{A'}$ has disappeared. We thus expect a bound which is roughly constant for these large masses. Moreover, we can derive a rough estimate for the bound by requiring $P_{\gamma \rightarrow A'}$ to be $\sim 10^{-4}$, the typical fractional uncertainty of the COBE-FIRAS measurement of the blackbody intensity. We thus get

$$\epsilon_{\text{est}} \sim 3 \times 10^{-8} \left(\frac{P_{\gamma \rightarrow A'}}{10^{-4}} \right)^{1/2} \left(\frac{10^{11}}{\mathcal{F}} \right)^{1/2} \quad (6)$$

A next-generation PIXIE-like experiment can in principle be sensitive to distortions on the order of 1 part in 10^8 , leading to a potential improvement of roughly two orders of magnitude in sensitivity to ϵ . However, this assumes perfect removal of foreground distortions from *e.g.* the epoch of reionization.

We stress that Eq. (6) merely represents a rough estimate for the constraint from CMB spectral distortions. While it gives a sense of the reach of such a probe, it is insufficient for obtaining the precise mass dependence of the bounds, and it has no information on the spectral shape of possible future signals. In the rest of our paper, we provide a thorough investigation of the CMB distortion caused by $\gamma \rightarrow A'$ oscillation using the Green's function method for the photon injection or removal process developed in Ref. [67].

III. SPECTRAL DISTORTIONS

In this section, we give a brief overview of how spectral distortions are generated in the CMB by exotic energy injection into photons. We intend only to introduce terminology that will be important for the reader to understand our method; for more in-depth discussions we invite the interested reader to consult the original, seminal works [88–93] or more recent papers such as Refs. [67, 94–99]. Before we begin the discussion, we want to emphasize that much of the existing literature has focused on pure energy injection or removal processes, *i.e.* processes that always conserve the comoving number density of photons. This can happen, for example, if the exotic process heats the baryons first, and the photons react to this change subsequently.² This is certainly not the case for $\gamma \rightarrow A'$ resonant conversions, and is the key reason why our results differ from Ref. [42]; however, we still follow existing conventions for clarity.

In the early universe, rapid scattering with electrons in the baryon plasma together with efficient photon-number-changing processes ensured that the photons were in thermal equilibrium with zero chemical potential. Photons therefore follow a blackbody distribution, *i.e.* their phase space density is given by \bar{f}_γ , where³

$$\bar{f}_\gamma(\omega, T) \equiv \frac{1}{e^{\omega/T} - 1}. \quad (7)$$

All thermodynamic properties of the photons are determined simply by its temperature T .

Once $T \lesssim$ keV, however, the rate of photon-number-changing processes in the energy range relevant to the measured CMB spectrum today drops below the Hubble expansion rate. After this point, any process that changes the number density and energy density of photons will drive the photon distribution away from the blackbody distribution, leading to a spectral distortion. Of course, if no such processes exists, then photons remain in a blackbody distribution throughout cosmological history, *i.e.* the photon phase space is $f_\gamma(x) = \bar{f}_\gamma(x)$ at all redshifts, where $x \equiv \omega/T$. We therefore define the spectral distortion $\Delta f(x)$ as the distortion to the blackbody distribution that we would observe

² This can in fact be highly unrealistic; any process that heats the baryons would also likely interact with photons at the same time. See Ref. [100] for a detailed study of the distortion produced by high-energy particles without making such an assumption.

³ We adopt the convention of defining phase space density excluding the degeneracy factor of 2 due to the spin states of the photon.

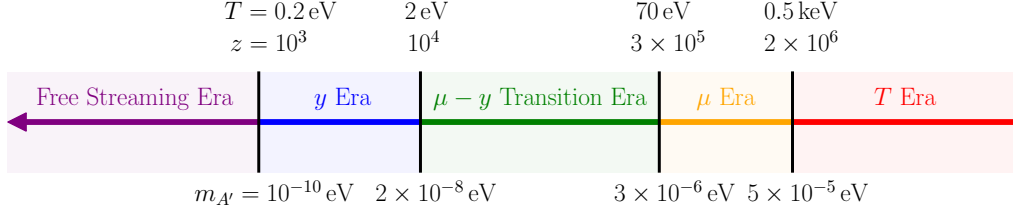


FIG. 2. The eras of the CMB spectral distortion. The redshifts separating different eras are located above the axis. The corresponding dark photon masses for the $\gamma \rightarrow A'$ resonant oscillation are shown are displaced below the axis. From today's universe to the earlier universe, there are five eras depending on the efficiency of CS, DCS, and BR: the free streaming era (purple), y -era (blue), μ - y transition era (green), μ -era (orange), and T era (red).

today, *i.e.* the phase space density that we observe today $f_\gamma(x)$ is given by

$$f_\gamma(x) = \bar{f}_\gamma(x) + \Delta f_\gamma(x). \quad (8)$$

The CMB phase space density has been measured by the FIRAS instrument aboard the COBE satellite in over 43 frequency bins ranging from $x \sim 1$ to $x \sim 10$. The FIRAS measurement confirmed that the CMB phase space density is consistent with a blackbody distribution, with a precision of 1 part in 10^4 , *i.e.* $\Delta f_\gamma / \bar{f}_\gamma \lesssim 10^{-4}$ in this frequency range. Any potential spectral distortion of interest can therefore be taken to be small.

The nature of the spectral distortion produced by any exotic energy injection process depends strongly on when these processes occur, and what scattering processes photons are undergoing efficiently at that time. The most relevant scattering processes are

$$\begin{aligned} \text{Compton Scattering (CS): } & e^- + \gamma \leftrightarrow e^- + \gamma, \\ \text{Double Compton Scattering (DCS): } & e^- + \gamma \leftrightarrow e^- + \gamma + \gamma, \\ \text{Bremsstrahlung (BR): } & e^- + X \leftrightarrow e^- + X + \gamma. \end{aligned} \quad (9)$$

Of these processes, DCS and BR are photon-number-changing. If they are efficient, *i.e.* have a rate much larger than the Hubble rate, they can drive the phase space density of photons rapidly toward a blackbody distribution, *i.e.* a Bose-Einstein distribution with zero chemical potential. On the other hand, CS is number conserving; it can still however redistribute photons and change their phase space distribution. The cosmological epoch for $T \lesssim \text{keV}$ can be divided into five main eras, according to how rapid these processes are. These are the T era $T \gtrsim 0.5 \text{ keV}$, μ -era $70 \text{ eV} \lesssim T \lesssim 0.5 \text{ keV}$, the μ - y transition era $2 \text{ eV} \lesssim T \lesssim 70 \text{ eV}$, the y -era $0.2 \text{ eV} \lesssim T \lesssim 2 \text{ eV}$, and the free-streaming era, $T \lesssim 0.2 \text{ eV}$. The corresponding redshifts separating these transitions and the value of $m_{A'}$ which would lead to a resonant conversion at these transitions are shown in Fig. 2.

The T era corresponds to $T \gtrsim 0.5 \text{ keV}$, when DCS and BR are highly efficient. These processes enforce thermal equilibrium and zero chemical potential in the photon distribution. Any arbitrary change to the phase space density away from a blackbody distribution by energy injection processes is quickly redistributed, resulting in a new blackbody distribution at a higher temperature. The characteristic distortion $\mathcal{T}(x)$ that is produced due to energy injection in this epoch is simply a temperature shift to the spectrum, and is defined as

$$T \text{ era: } \Delta f_\gamma(x) \equiv \bar{f}_\gamma(\omega, T + tT) - \bar{f}_\gamma(\omega, T) \simeq \bar{f}_\gamma(x) t\mathcal{T}(x), \quad (10)$$

where $t \ll 1$ determines the size of the distortion. Expanding to linear order in t shows that

$$\mathcal{T}(x) = \frac{x e^x}{e^x - 1}. \quad (11)$$

Note that such a distortion is fundamentally unobservable, because the blackbody temperature observed today T_0 is a free parameter in Λ CDM cosmology, and can always be adjusted to absorb any unexpected energy injection processes happening during the T era. The impact of exotic energy injection processes on the CMB spectrum are therefore only observable if they occur after the T era.

In the μ -era ($70\text{ eV} \lesssim T \lesssim 0.5\text{ keV}$), DCS and BR become inefficient, while CS still remains highly efficient. Immediately after any energy injection process, CS rapidly drives photons to thermal equilibrium, *i.e.* its phase space density will approach a Bose-Einstein distribution. However, the lack of number-changing-processes means that the comoving number density of photons after the injection process is conserved, and the equilibrium distribution reached will in general have a nonzero chemical potential. Injection processes can also cause a temperature shift as in the T era. The spectral distortion in this era can be written as

$$\mu \text{ era: } \Delta f_\gamma(x) = \bar{f}_\gamma(\omega + \mu T, (1+t)T) - \bar{f}_\gamma(\omega, T). \quad (12)$$

We can likewise expand in μ and t to obtain the following conventional form for the distortion:

$$\Delta f_\gamma(x) \simeq \bar{f}_\gamma(x) [\mu \mathcal{M}(x) + (t - \alpha_\mu \mu) \mathcal{T}(x)], \quad (13)$$

where

$$\mathcal{M}(x) \equiv \mathcal{T}(x) \left(\alpha_\mu - \frac{1}{x} \right), \quad (14)$$

and $\alpha_\mu \simeq 0.456$.⁴ $\mathcal{M}(x)$ is typically called the μ -distortion, and μ specifies the size of this distortion.

In the y -era ($0.2\text{ eV} \lesssim T \lesssim 2\text{ eV}$), CS becomes too slow for photons to remain in thermal equilibrium, *i.e.* the photon phase space density does not approach a Bose-Einstein distribution any longer. However, CS is still rapid enough that photons do scatter with baryons, allowing some limited redistribution of the photons. In a pure energy injection process, where energy is dumped into heating the baryons, blackbody photons undergo CS with the baryons, producing a y -distortion:

$$y \text{ era, pure energy injection: } \Delta f_\gamma(x) = \bar{f}_\gamma(x) y \mathcal{Y}(x), \quad (15)$$

with $y \ll 1$, and where

$$\mathcal{Y}(x) = \mathcal{T}(x) \left(x \frac{e^x + 1}{e^x - 1} - 4 \right). \quad (16)$$

We stress, however, that for general energy injection processes with photons being injected or removed, the distortion is generally significantly more complicated. The transition between the μ and y -eras ($2\text{ eV} \lesssim T \lesssim 70\text{ eV}$) is also an epoch where the evolution of photons is complicated, and requires a numerical treatment, even in the case of pure energy injection [99].

After recombination, the majority of photons effectively never scatter with baryons ever again. During this free-streaming era ($T \lesssim 0.2\text{ eV}$), any distortion to the CMB, *e.g.* from $\gamma \rightarrow A'$ resonant conversion, remains frozen in place, and photons are unable to redistribute themselves to any significant extent.⁵

⁴ The convention adopted here includes the factor of $\alpha_\mu \mathcal{T}(x)$ in the definition of $\mathcal{M}(x)$. This originates from the fact that for a pure energy injection with no injection of photons, one can derive $t = \alpha_\mu \mu$, and so $\mathcal{M}(x)$ accounts for the full distortion. This relation does not hold, however, if the photon number changes during the injection, but we still follow this convention for consistency of notation.

⁵ There are some small spectral distortions expected even in standard cosmology, such as the y -distortion that will be imprinted in the CMB due to scattering with free electrons after reionization, which should leave a 10^{-6} level distortion, well below the FIRAS uncertainty.

IV. GREEN'S FUNCTION METHOD

In this section, we give an introduction to computing the CMB spectral distortion utilizing the Green's function method, outlined in Ref. [67]. First, we define the CMB intensity,

$$I_\gamma(\omega_0; T_0) \equiv \frac{dP_\gamma}{dA d\Omega d\nu_0} = \frac{\omega_0^3}{2\pi^2} f_\gamma(\omega_0, T_0). \quad (17)$$

Here, we follow the convention of radio astronomy. P_γ is the power of the CMB photon received by the antenna, Ω is the solid angle along the line-of-sight, A is the antenna's projected area with respect to the line-of-sight, and $\nu_0 = \omega_0/2\pi$ is the frequency of the received CMB photons. When there is no distortion, the CMB intensity is $\bar{I}_\gamma(\omega_0; T_0) = (\omega_0^3/2\pi^2)\bar{f}_\gamma(\omega_0, T_0)$. The distortion of the phase space distribution of the CMB photon leads to the distortion of the CMB intensity away from \bar{I}_γ . The commonly used unit of CMB intensity is $\text{Jy sr}^{-1} = 10^{-26} \text{ W m}^{-2} \text{ Hz}^{-1} \text{ sr}^{-1}$, in agreement with the units expected from Eq. (17).

To compute the spectral distortion due to $\gamma \rightarrow A'$, we adopt the Green's function approach described in Ref. [67]. If photons are injected or removed at some frequency x' at some redshift z' , this ultimately produces a distortion in intensity with some characteristic shape $G(x; x', z')$ that we observe today at frequency x (we use $'$ to denote quantities related to the injection, while variables without $'$ refer to quantities today). If the number of photons that are injected or removed is small, the total distortion can be treated linearly, and is simply an integral of $G(x; x', z')$ over all values of x' and z' , weighted by how much was injected at x' and z' [67]. $G(x; x', z')$, when appropriately normalized, is precisely the Green's function mapping energy injection at x' and z' to a characteristic distortion.

We now make this intuitive explanation precise. Let $S(x', z')$ be the ratio of the number density of photons injected with frequencies between x' and $x' + dx'$ in the redshift interval between z' and $z' + dz'$, to the number density of all photons at z' . Then the Green's function $G(x; x', z'; T_0)$ is defined as

$$\Delta I_\gamma(x; T_0) = \int dz' \int dx' G(x; x', z'; T_0) S(x', z'), \quad (18)$$

which has the usual structure of a solution using the Green's function method, with S acting as a source term. ΔI_γ is the distortion to the CMB intensity as observed today. With this definition, G has units of intensity as well. ΔI_γ and G depend on T_0 , which we allow to float in our data analysis: see Appendix A for more details on this. In the context of $\gamma \rightarrow A'$ conversions,

$$S(x', z') = -\frac{1}{\bar{n}_\gamma} \frac{d\bar{n}_\gamma}{dx'} P_{\gamma \rightarrow A'}(x') \delta(z' - z'_{\text{res}}), \quad (19)$$

where $P_{\gamma \rightarrow A'}$ is defined in Eq. (4), and z'_{res} is the redshift at which the resonant conversion happens. The negative sign is consistent with the fact that photons are removed by $\gamma \rightarrow A'$ conversions. Note that $(d\bar{n}_\gamma/dx')/\bar{n}_\gamma = (1/2\zeta(3)) x'^2/(e^{x'} - 1)$ is redshift invariant; we can therefore integrate over redshift to find

$$\Delta I_\gamma(x; T_0) = - \int dx' \frac{1}{\bar{n}_\gamma} \frac{d\bar{n}_\gamma}{dx'} P_{\gamma \rightarrow A'}(x') G(x; x', z'_{\text{res}}; T_0). \quad (20)$$

We can also show that the Green's functions obey the following normalization condition:

$$2T_0 \int dx G(x; x', z'; T_0) = x' \alpha_\rho \bar{\rho}_\gamma(T_0), \quad (21)$$

where $\bar{\rho}_\gamma(T_0)$ is the energy density of the CMB today, and $\alpha_\rho \simeq 0.3702$, defined in Appendix B. This is in agreement with Ref. [67]; we derive this normalization condition for completeness in Appendix D 2, which essentially comes from requiring energy conservation during the photon injection/removal process.

Ref. [67] provides analytic expressions for G in the μ and y -eras. In the μ -era, the Green's function G_μ for computing

the μ -distortion is

$$G_\mu(x; x', z'; T_0) = \alpha_\rho x' \cdot \frac{3}{\kappa_c} \mathcal{J}^*(z') \left[1 - P_s(x', z') \frac{x_0}{x'} \right] \mathbf{M}(x; T_0) + \frac{\lambda(x', z')}{4} \mathbf{T}(x; T_0), \quad (22)$$

where $\mathbf{M} = \bar{I}_\gamma \cdot \mathcal{M}$ and $\mathbf{T} = \bar{I}_\gamma \cdot \mathcal{T}$, and $x_0 \simeq 3.6$. We provide the concrete derivation of Eq. (22) in Appendix C for readers with further interest. $P_s(x', z')$ is the probability that a photon injected with frequency x' at redshift z' survives before the distribution relaxes into a quasi-stationary phase—injected photons can be absorbed by DCS or BR before CS redistributes them, contributing instead to the heating of baryons [67]. In the limit of $P_s \rightarrow 0$, this reduces to a pure energy injection/removal process; $P_s > 0$ includes the possibility of increasing or decreasing the comoving number density of photons. \mathcal{J}^* is the visibility function accounting for the washout effect of DCS and BR on the μ -type distortion. λ is a coefficient in front \mathbf{T} , which is set by the normalization condition of the Green's function Eq. (21). The concrete formula of λ can be found in Eq. (D10). The definitions and the numerical values of the other constants, such as α_ρ and κ_c , are worked out in Appendix B. As we argued in Sec. III, because we treat T_0 as a nuisance parameter when analyzing the data of CMB intensity, \mathbf{T} is fundamentally unobservable. Therefore, we simply drop the second term containing \mathbf{T} in Eq. (22) from the Green's function, with the only observable part of the distortion coming from the first term containing \mathbf{M} .⁶ When $T \gg 0.5$ keV, $\mathcal{J}^* \simeq 0$ because DCS and BR are efficient enough to set the chemical potential of the CMB photon to zero. In this situation, there is no observable CMB spectral distortion.

An analytic expression for the Green's function during the y -era, G_y , is also derived in Ref. [67]; the full expression and other important aspects of G_y are discussed in Appendix D 4. Here, to give some physical intuition, we only show the approximate form of G_y in the limit where CS is very inefficient. To describe the efficiency of CS, the following dimensionless quantity is defined

$$y_\gamma(z) = \int_0^z dz' \frac{T(z')}{m_e} \frac{\sigma_T n_e(z')}{H(z')(1+z')}, \quad (23)$$

where σ_T is the Thomson scattering cross-section. y_γ is a measure of the efficiency of energy transfer to the photon due to Compton scattering.⁷ In the late universe, especially the y -era and free-streaming era, $y_\gamma \ll 1$, *i.e.* CS is inefficient at significantly changing the energy of a photon. In this situation, G_y can be approximately written as

$$G_y(x; x', z'; T_0) \simeq \alpha_\rho x' \cdot (1 - P_s(x', z')) \frac{\mathbf{Y}(x; T_0)}{4} + \alpha_\rho x' \cdot \frac{\bar{\rho}_\gamma(T_0)}{2T_0} P_s(x', z') \delta(x - x'), \quad (24)$$

where $\mathbf{Y} = \bar{I}_\gamma \cdot \mathcal{Y}$. In Eq. (24), the first term leads to a y -distortion due to heating from the absorption of photons, while the second term leads to a free-streaming distortion, where injected photons simply redshift. In the full expression for G_y , shown in Eq. (D12), the $\delta(x - x')$ in the second term of Eq. (24) is not an exact delta function but is broadened by CS into a Gaussian with respect to $\log x$ with width $\sim \sqrt{y_\gamma} x'$. This effect is more pronounced for large x' or at earlier epochs where the CS is more efficient. The reader should refer to Appendix D 4 for more detailed discussions.

In the μ - y transition era, there is no analytic form for the Green's function available. In order to perform a fully accurate determination of the spectral distortion, a full numerical treatment using a code package like CosmoTherm [97] is needed to track how the CMB spectrum evolves during this era. Since there is no publicly available package for computing spectral distortions, we have to instead rely on approximations. We know that the Green's function should tend toward the Green's functions of the μ - or y -eras at higher or lower z' , and therefore we parametrize

$$G_{\text{trans}}(x; x', z'; T_0) = \mathcal{T}_\mu(x', z') \cdot G_\mu(x; x', z'; T_0) + \mathcal{T}_y(x', z') \cdot G_y(x; x', z'; T_0), \quad (25)$$

which smoothly connects Green's functions in the μ and y -eras; as we approach the μ -era $\mathcal{T}_\mu \simeq 1$ and $\mathcal{T}_y \simeq 0$, while $\mathcal{T}_\mu \simeq 0$, $\mathcal{T}_y \simeq 1$ as we approach the y -era.

⁶ Of course, we could have subtracted any multiple of \mathbf{T} from the expression by the same argument; this is merely a way to simplify the expression for G_μ .

⁷ Note that since we are in the regime where $T \ll m_e$, Compton scattering $e^- + \gamma \rightarrow e^- + \gamma$ simply reduces to Thomson scattering. The fraction of energy transferred to the photon during each Thomson scattering event is $\sim T/m_e$, which appears as the first term in the integral.

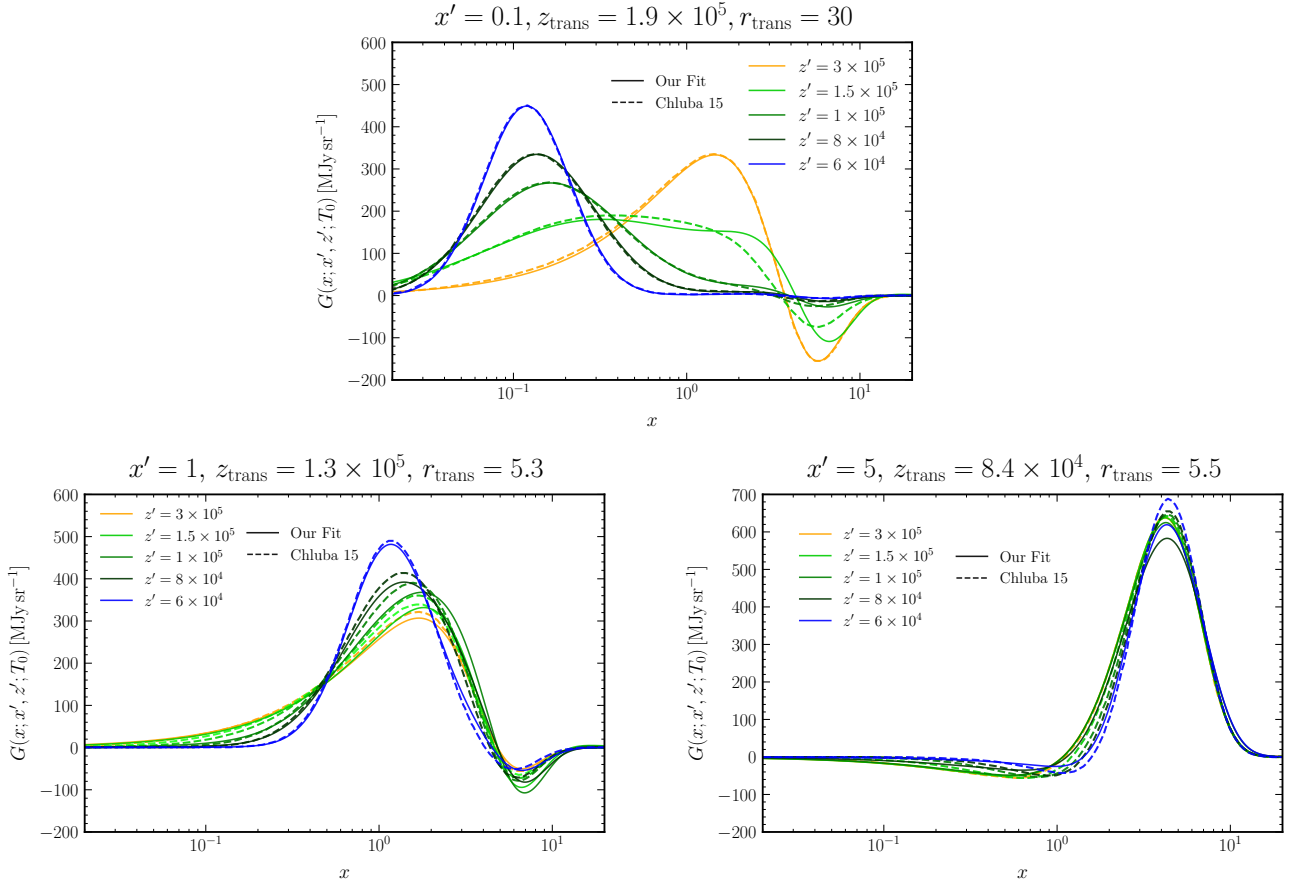


FIG. 3. The fitted Green's functions (solid lines) for the μ - y transition era listed in Eq. (25) with different frequencies x' and different redshifts z' , compared with the numerically computed Green's functions obtained in Ref. [67] (dashed lines). Here, for each x' , we find the best fit values of z_{trans} and r_{trans} compared with Ref. [67]. When $z' \leq 6 \times 10^4$, we have $G \simeq G_y$, which is labeled by the solid blue line. When $z' \geq 3 \times 10^5$, we have $G \simeq G_\mu$, which is labeled by the solid orange line. The shapes of the Green's functions in the intermediate epoch where $6 \times 10^4 < z < 3 \times 10^5$ are represented by the green lines with different darkness.

For the fiducial treatment that we adopt in this paper, the form of $\mathcal{J}_\mu(x', z')$ that we adopt is the same as that of a similar function used to determine the Green's functions for spectral distortions from pure energy injection in the same era [99]:

$$\mathcal{J}_\mu(x', z') = 1 - \exp \left[- \left(\frac{1 + z'}{1 + z_{\text{trans}}(x')} \right)^{r_{\text{trans}}(x')} \right], \quad (26)$$

where z_{trans} represents the redshift at which the Green's function transits from G_μ to G_y , and r_{trans} represents how rapidly such a transition happens. To maintain the proper normalization of the Green's function as required by Eq. (21), we must always have

$$\mathcal{J}_y(x', z') = 1 - \mathcal{J}_\mu(x', z'). \quad (27)$$

In Eq. (26), we take z_{trans} and r_{trans} to be x' -dependent parameters, fitting for them at six discrete values: $x' = 10^{-3}, 10^{-2}, 10^{-1}, 1, 5, \text{ and } 15$. For each value of x' , we find the values of z_{trans} and r_{trans} that minimize the function

$$\mathcal{D}(z_{\text{trans}}, r_{\text{trans}}; x') = \int_{-\infty}^{+\infty} d \log x \sum_i \left| G(x; x', z'_i; z_{\text{trans}}, r_{\text{trans}}) - \tilde{G}(x; x', z'_i) \right|^2, \quad (28)$$

where G is as defined in Eq. (25) with \mathcal{T}_μ given in Eq. (26), and \tilde{G} is the numerically computed Green's functions over all z'_i reported in Ref. [67]. The sum corresponds to adding up the contributions to \mathcal{D} for each reported Green's function at the redshifts z'_i . The best fit values of $(z_{\text{trans}}, r_{\text{trans}})$ that we obtain for each x' are

$$\left\{ \begin{array}{l} x' = 10^{-3} : z_{\text{trans}} = 3.1 \times 10^5, r_{\text{trans}} = 3.3 \\ x' = 10^{-2} : z_{\text{trans}} = 2.3 \times 10^5, r_{\text{trans}} = 7.1 \\ x' = 10^{-1} : z_{\text{trans}} = 1.9 \times 10^5, r_{\text{trans}} = 30 \\ x' = 1 : z_{\text{trans}} = 1.3 \times 10^5, r_{\text{trans}} = 5.3 \\ x' = 5 : z_{\text{trans}} = 8.4 \times 10^4, r_{\text{trans}} = 5.5 \\ x' = 15 : z_{\text{trans}} = 10^5, r_{\text{trans}} = 2.5 \end{array} \right. . \quad (29)$$

For $x' = 0.1$, we find that the fit prefers a sudden transition between μ -type and y -type Green's functions, which occurs at large r . Finding no significant change to the fit once $r_{\text{trans}} \geq 30$, we simply choose $r_{\text{trans}} = 30$. To get z_{trans} and r_{trans} for intermediate values of x' , we linearly interpolate over $\log z_{\text{trans}}$ and $\log r_{\text{trans}}$ as a function of $\log x'$.

The resulting fits for $G_{\text{trans}}(x; x', z'; T_0)$ for $x' = 0.1, 1, \text{ and } 5$ and the comparison with Ref. [67] are shown in Fig. 3. Choices of z' that are closer to the y -era are shown in blue, while those that are closer to the μ -era are shown in orange. Comparing these results with the numerically computed Green's functions in the μ - y transition shown in Ref. [67], we find good quantitative agreement for these particular choices of z_{trans} and r_{trans} , with the relative difference between our approximate Green's functions and those shown in Ref. [67] being less than 30% in the region where $0.1 \leq x' \leq 5$, across all values of z' and x considered. For $x' < 0.1$ or $x' > 5$, energy injection from $\gamma \rightarrow A'$ resonant conversion of photons in these ranges do not contribute significantly to ΔI_γ . This is because at low x' , the fraction of energy removed from the CMB by $\gamma \rightarrow A'$ per $\log x'$ interval scales as x'^2 , while at large x' , the CMB becomes exponentially suppressed, and yet again only a small fraction of energy is removed. Given that the error of the fitting in these marginal regions are less than 50%, the full numerical error from integrating over these regions is at most at the 5% level.

So far, we have discussed the procedure we use to set our fiducial limits in the μ - y transition era. To further quantify the uncertainty associated with our approximate treatment of the transition era, we also adopt Green's functions in the μ - y transition era with different values of constant z_{trans} and r_{trans} , *i.e.* with no x' dependence. To be more specific, we calculate the CMB spectral distortion over the following constant values of z_{trans} and r_{trans} : $z_{\text{trans}} = \{5.8 \times 10^4, 10^5, 1.4 \times 10^5\}$ and $r_{\text{trans}} = \{1.88, 3, 5\}$. These values were chosen to satisfy the following criteria: 1) $\Delta I_\gamma^{\text{trans}} \simeq \Delta I_\gamma^\mu$ when $z_{\text{res}} = 3 \times 10^5$, so that the Green's function transitions smoothly to the μ -era Green's function as z approaches the μ -era, and 2) $y_\gamma \lesssim 1$ at $z = z_{\text{trans}}$, since $y_\gamma \gg 1$ characterizes the μ -era when CS is highly efficient. These other versions of the Green's functions will be used to assess how dependent the limits are on the approximation made in the μ - y transition range of $m_{A'}$ masses.

V. SPECTRAL DISTORTION FROM $\gamma \rightarrow A'$ AND COBE-FIRAS CONSTRAINTS

The Green's function method described in the previous section allows the computation of the spectral distortions associated with any photon injection/removal process. We can now compute the $\Delta I_\gamma(x; T_0)$ associated with photon-dark photon oscillation using Eq. (20), given ϵ and $m_{A'}$. We then compare the predicted CMB spectrum with the spectral distortion from $\gamma \rightarrow A'$ with the intensity of the CMB measured by the FIRAS instrument aboard COBE [49]. To set a limit on ϵ for each value of $m_{A'}$, we perform a profile likelihood test, constructing a test statistic from the profile likelihood ratio with model parameter ϵ and nuisance parameter T_0 . The Gaussian likelihood that we use is constructed from the full covariance matrix provided by the COBE-FIRAS experiment [49]. Further details of the statistical analysis are given in Appendix A.

We begin by showing the main result of our analysis, the 95% confidence limit on ϵ as a function of $m_{A'}$, in Fig. 4, before discussing various details of the result. The solid colored line is our fiducial constraint at the 95 % confidence level on the dark photon mixing parameter ϵ for a broad range of dark photon masses in the ultralight region. Different colors represent the $\gamma \rightarrow A'$ -induced spectral distortions happening in different epochs; the free-streaming era, y -era,

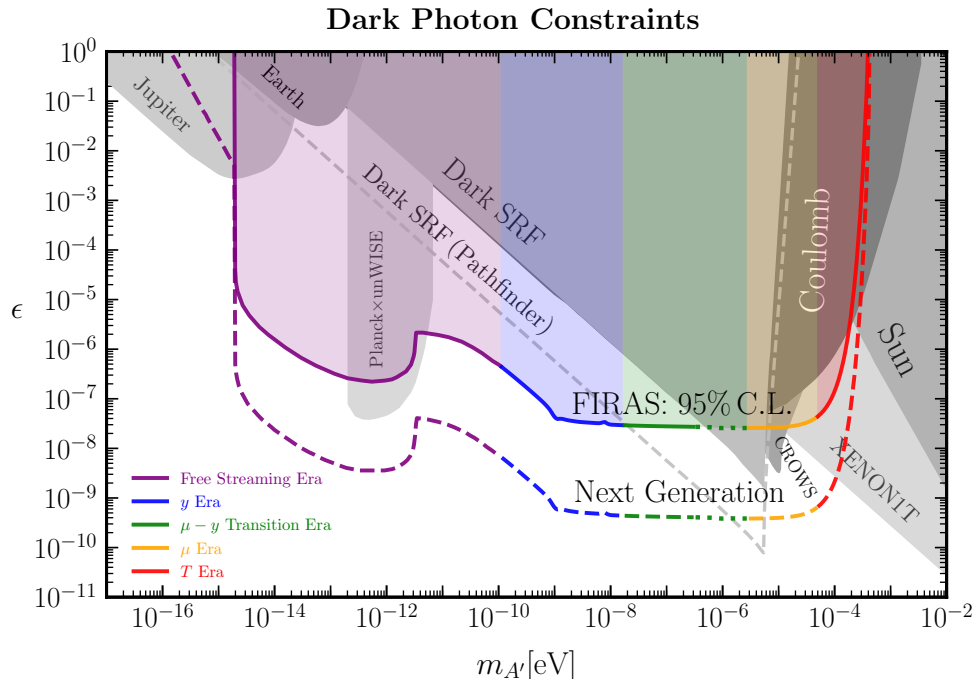


FIG. 4. The dark photon constraints and projections from CMB spectral distortion. The solid colored line is the CMB constraint from the COBE-FIRAS dataset at the 95% confidence level. The dashed colored line is the future projection from a next-generation experiment with a sensitivity 10^4 better than FIRAS, and assuming perfect foreground removal. Different colors represent different experiment stages of the CMB spectral distortion. The free-streaming era, y -era, μ - y transition era, μ -era, and T -era are denoted by purple, blue, green, orange, and red, respectively. Results from the free-streaming era (purple) are identical to Ref. [43]. The dotted line shows where the uncertainty associated with the Green’s function approximation in the μ - y transition era is important. Other constraints from DarkSRF [68], CROWS [5], Coulomb [1–4], XENON1T [16, 18], Sun [21–24, 26], Jupiter [31–33], Earth [3, 32, 34–36] are labeled and shown in gray. We show the future projection of the DarkSRF (Pathfinder) with the gray dashed line [6]. Conservative limits from Planck CMB power spectrum data derived in Ref. [47] found limits that are slightly weaker than those derived from COBE-FIRAS [43, 58] and are therefore not shown, while a separate study found strong limits at $m_{A'} \sim 10^{-12}$ eV using a cross correlation of Planck and unWISE data [48] (shown in gray, labeled Planck \times unWISE).

μ - y transition era, μ -era, and T era are denoted by purple, blue, green, orange, and red, respectively. The results for the free-streaming era shown in purple are identical to those found in Ref. [43]; the limits for the other regimes constitute new limits worked out in this paper. The dashed colored line is the projected reach for a next-generation satellite, such as PIXIE [101, 102]. We estimate the reach by assuming a 10^4 improvement in the sensitivity to distortions, and assume we are able to remove foreground contributions to the CMB spectral distortion such as from reionization accurately, leaving a detailed analysis of foreground removal and the exact detector performance to future work. The green line denotes the μ - y transition region, in which we used the approximation scheme described in Eq. (25). When the line is solid, we expect our approximation scheme to be highly robust, while the dashed line indicates the result obtained by our fiducial treatment. Further discussion on this region will appear at the end of this section.

In gray, we show constraints from other probes, such as the DarkSRF [68], CROWS [5], modifications to Coulomb’s law [1–4], XENON1T [16, 18], the Sun [21–24, 26], Jupiter’s magnetic field [31–33], and the Earth’s magnetic field [3, 32, 34–36]. In addition, the CMB power spectrum has also recently been shown to provide strong limits on the dark photon. Ref. [47] found conservative limits based on Planck data that are slightly weaker than limits from FIRAS data [43, 58], while cross-correlation between Planck and unWISE [48] gives the leading limits for $m_{A'} \sim 10^{-12}$ eV. We also show the future pathfinder projection of the Dark SRF with the gray dashed line [6]. Among all the current experimental methods, the CMB spectral distortion stands out as one of the most sensitive methods in the

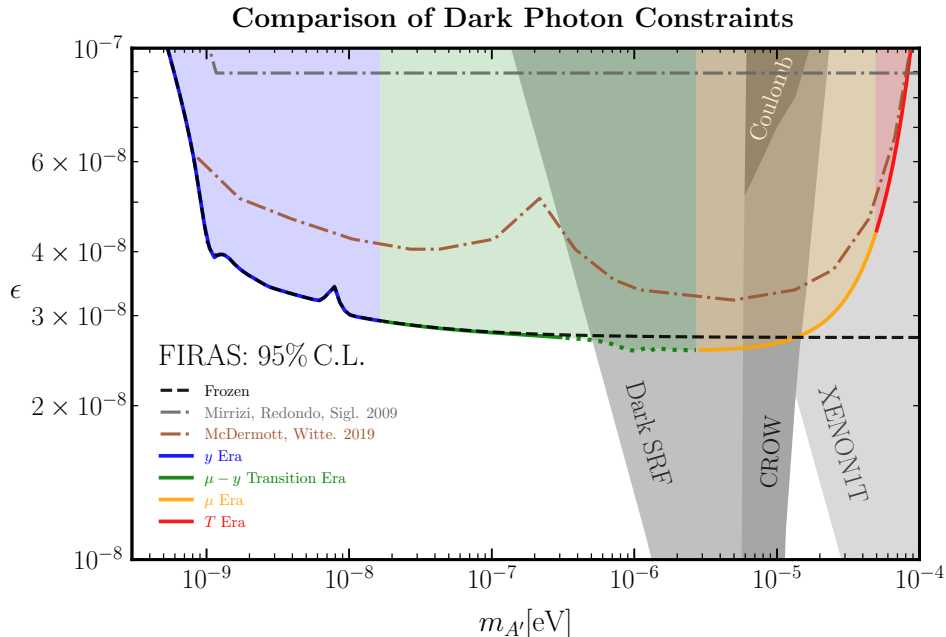


FIG. 5. Comparison of our fiducial constraint (rainbow colored line) with previous results. The dash-dotted gray line and the dash-dotted brown line are the constraints obtained using the free streaming calculation of Ref. [39], and assuming that the effect of $\gamma \rightarrow A'$ is a pure energy removal process [42], respectively. We repeated the free streaming calculation with the free electron fraction taken from CLASS [104, 105] based on Planck 2018 data, and show the result as the black dashed line.

10^{-15} eV – 10^{-6} eV mass range, even with the COBE-FIRAS dataset acquired three decades ago. Future projections of DarkSRF show strong sensitivity to dark photons with a mass in the range of 10^{-8} eV– 10^{-5} eV. Future light-shining-through-wall experiments [7–10] and the next generation helioscope [14] are also projected to probe new parameter space for $m_{A'} \gtrsim 10^{-5}$ eV. That being said, a next-generation CMB spectrum experiment will be one of the most effective methods for testing this region of parameter space as well.

As we enter the T -era in the red region of the plot, the distortions due to $\gamma \rightarrow A'$ become primarily an unobservable shift in the temperature, leaving only a small detectable μ -type distortion; this explains the exponential loss of sensitivity in this region. Note that based on our estimate in Eq. (6), once $\epsilon \gtrsim 3 \times 10^{-7}$, the probability of conversion $P_{\gamma \rightarrow A'}$ for $x \sim 1$ starts to exceed 1%, and the Green’s function assumption of small distortions breaks down. Although a more detailed treatment of large distortions, as described in Ref. [103], can be used to get accurate limits in the T -era with $\epsilon \gtrsim 3 \times 10^{-7}$, existing constraints from *e.g.* XENON1T [16, 18] ($\epsilon \sim 2 \times 10^{-9}$ for $m_{A'} \sim 10^{-4}$ eV) far supersede any potential limits from FIRAS or a next-generation CMB spectrum measurement, rendering a careful treatment unnecessary.

Fig. 5 shows a zoomed-in version of Fig. 4, as well as a comparison of our new COBE-FIRAS limits with previous results. The notch seen in our constraints at $m_{A'} \sim 10^{-8}$ eV is due to HeIII to HeII recombination happening at $z \sim 6000$. At this point, $|dm_{\gamma}^2/dz|$ is larger than those at nearby redshifts. Therefore, $P_{\gamma \rightarrow A'}$ is suppressed according to Eq. (4), which slightly alleviates the COBE-FIRAS constraint at this value of $m_{A'}$. The dot-dashed gray line shows the result from Ref. [39]. These results assumed that photons were free-streaming even before recombination. They also did not take the evolution of the free electron fraction x_e into account accurately, resulting in an $m_{A'}$ -independent limit, due to the approximate result for $P_{\gamma \rightarrow A'}$ that we derived in Eq. (5). Updating their result with x_e calculated from CLASS [104, 105] using Planck 2018 cosmology [84], but still assuming free-streaming, leads to the black dashed curve. We see that free-streaming is an excellent approximation for $m_{A'} \leq 10^{-7}$ eV, but starts to deviate from the actual results above this mass. In particular, we need the full machinery of the Green’s function method to calculate how the limit relaxes at high masses.

The dash-dotted brown line shows the result from Ref. [42], which assumes that the effect of $\gamma \rightarrow A'$ is equivalent

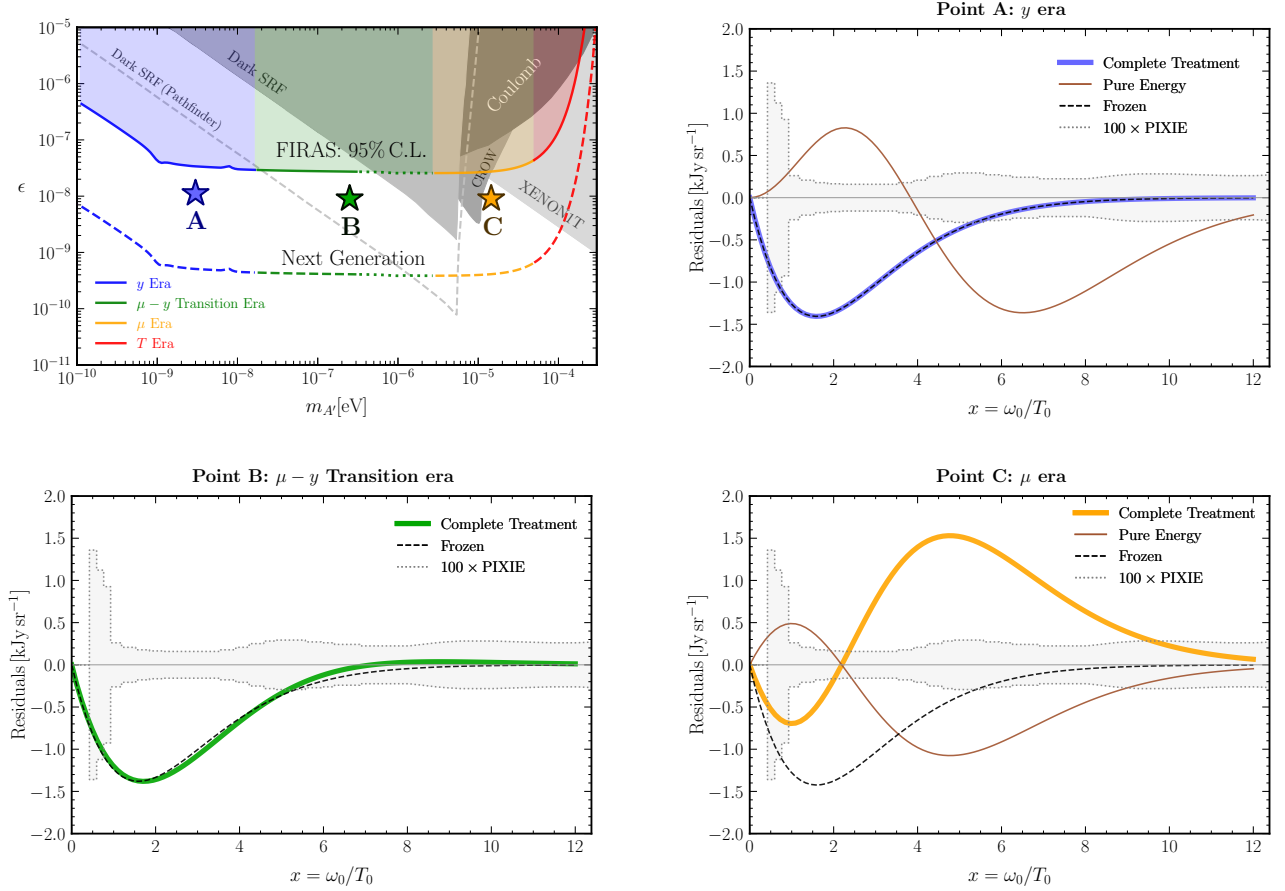


FIG. 6. (Top left) Parameter points A, B and C as a function of $m_{A'}$ and ϵ , and the CMB spectral distortion caused by $\gamma \rightarrow A'$ happening in points A (top right, y -era), B (bottom left, μ - y transition era), and C (bottom right, μ -era). We plot the predicted CMB spectral distortion using our method (thick lines with the same colors as corresponding eras) labeled by the “completed treatment”, the method assuming just free-streaming, labeled “frozen” (black dashed lines), and the method assuming the spectral distortion is given by a pure energy removal (thin solid brown lines) for a direct comparison with Ref. [42]. This latter did not include a specific treatment for the μ - y transition era. Therefore, for point B we do not show the pure energy injection curve. The computed distortions is to be compared with the projected sensitivity of PIXIE [102], which has been scaled up by a factor of 100 in these plots (dotted lines)

to a pure energy removal process, producing μ - and y -type distortions in their respective eras. They then directly recast the COBE-FIRAS constraints on $|\mu|$ and $|y|$ parameters to the dark photon parameter space. This assumption is also inaccurate: the actual distortion differs significantly from a pure μ - or y -type distortion, as we will discuss in detail below. Furthermore, Ref. [42] did not attempt to treat the μ - y transition period consistently, leading to an artificial notch at around $m_{A'} \sim 2 \times 10^{-7}$ eV.

Importantly, the shape of the spectral distortion predicted by our more complete treatment differs significantly from the distortion expected from either Ref. [39] or Ref. [42]. In Fig. 6, we show the spectral shape of a residual signal for a resonant conversion happening at three benchmark points: point “A” in the y -era (blue, top right), point “B” in the μ - y transition era (green, bottom left), and point “C” in the μ -era (yellow, bottom right). We choose ϵ to be roughly three times smaller than the COBE-FIRAS constraint that we set in parameter space that is currently not ruled out. In these three panels, the thick solid lines labeled by “complete treatment” are the shapes of the CMB spectral distortions acquired in our work. We compare this to the CMB spectral distortion assuming free-streaming photons after $\gamma \rightarrow A'$ conversion (dashed black, labeled “Frozen”, utilized in Ref. [39]) and the one assuming that $\gamma \rightarrow A'$ induces a pure energy removal (solid brown, labeled “Pure Energy”, utilized in Ref. [42]). We also include the

expected sensitivity from PIXIE [102], scaled up by a factor of 100, to highlight the impact a next-generation CMB spectrum satellite would have on detecting A' .

At point ‘‘A’’, resonant $\gamma \rightarrow A'$ conversion happens in the y -era. From the upper right panel of Fig. 6, we find that the spectral distortion shape from the complete treatment (thick solid blue) is similar to the result under the assumption that photons free-stream after $\gamma \rightarrow A'$ conversion (dashed black). It is instructive to see how taking the appropriate limit of G_y in our calculations reproduces the distortion from simple free-streaming at low redshifts. Because $P_s \simeq 1$ in the relevant frequency range, the free-streaming term in Eq. (24) dominates over the \mathbf{Y} -term. Moreover, because $y_\gamma \ll 1$, the delta-function approximation that we used in Eq. (24) is legitimate (this is the correct limit obtained by taking the more general Green’s function found in Eq. (D12) and applying the narrow width approximation). Based on the discussions above, we can substitute Eq. (24) into Eq. (18) to obtain

$$y \text{ era: } \Delta I_\gamma^y(x; T_0) \simeq -P_{\gamma \rightarrow A'}(x) \bar{I}_\gamma(x; T_0), \quad (30)$$

which is the same as the result assuming that photons only free-stream after the resonant $\gamma \rightarrow A'$ conversion. This result explains the smooth transition from our COBE-FIRAS constraint to the one shown in Ref. [43] when $m_{A'} \lesssim 10^{-10}$ eV. One should also note that naively assuming that spectral distortions imparted on the CMB by $\gamma \rightarrow A'$ are equivalent to pure energy removal, as utilized in Ref. [42], leads to the incorrect shape of the CMB distortion. This treatment is equivalent to setting $P_s \simeq 0$ in our expression for G_y , such that $\Delta I_\gamma(x; T_0)|_{\text{pure energy}} \propto \mathbf{Y}(x; T_0)$ instead. Therefore, the COBE-FIRAS constraint in Ref. [42] cannot smoothly transit to the low mass limits in Ref. [43] when $m_{A'} \lesssim 10^{-10}$ eV. This highlights the importance of doing the more accurate calculation that we perform in this paper.

The point ‘‘C’’ corresponds to the $\gamma \rightarrow A'$ resonant conversion in the μ -era. From the lower right panel of Fig. 6, we find that the CMB spectral distortion (thick solid orange) has a similar shape to the \mathbf{M} -function, but has the opposite sign as compared to the result assuming the spectral distortion comes from just pure energy removal (solid brown) utilized in Ref. [42]. To quantitatively explain this, we can write the μ -era distortion as

$$\mu \text{ era: } \Delta I_\gamma^\mu(x; T_0) = \mu_{\gamma \rightarrow A'} \mathbf{M}(x; T_0), \quad (31)$$

where

$$\mu_{\gamma \rightarrow A'} \simeq -\alpha_\rho \frac{3}{\kappa_c} \mathcal{J}^*(z_{\text{res}}) \epsilon^2 \mathcal{F} \left(1 - \left\langle P_s(x', z_{\text{res}}) \frac{x_0}{x'} \right\rangle \right). \quad (32)$$

Here, $x_0 \simeq 3.6$, and

$$\langle f(x') \rangle = \int dx' \frac{1}{\bar{n}_\gamma} \frac{d\bar{n}_\gamma}{dx'} f(x'), \quad (33)$$

which is intuitively an average of $f(x')$ over the spectrum of photons. As we have discussed in Sec. IV, the temperature shift term of Eq. (22) can be removed because T_0 is a nuisance parameter varied during the data analysis. Here, we approximately have $P_{\gamma \rightarrow A'} \simeq \epsilon^2 \mathcal{F}/x'$ based on Eq. (5). In the frequency range and redshift we are interested in, we find that $P_s \simeq 1$. Therefore, we have

$$\mu_{\gamma \rightarrow A'} \propto - \left(1 - \left\langle \frac{x_0}{x'} \right\rangle \right) > 0. \quad (34)$$

This result is completely different from the spectral distortion calculated under the pure energy removal formalism assumption, as used in Ref. [42]. The pure energy removal process is recovered in the limit where no photon survives and everything cools the plasma, *i.e.* $P_s \simeq 0$, from which we obtain $\mu_{\gamma \rightarrow A'}|_{\text{pure energy}} < 0$, which has the opposite sign. This explains the apparent sign flip in the bottom right plot of Fig. 6.

The bottom left plot of Fig. 6 corresponds to point ‘‘B’’, with $\gamma \rightarrow A'$ happening in the μ - y transition era. The CMB spectral distortion (thick blue line) is then obtained by plugging the Green’s function Eq. (25) in Eq. (20)

$$\mu - y \text{ transition era: } \Delta I_\gamma^{\text{trans}}(x; T_0) = - \int dx' \frac{1}{\bar{n}_\gamma} \frac{d\bar{n}_\gamma}{dx'} P_{\gamma \rightarrow A'}(x') G_{\text{trans}}(x; x', z'_{\text{res}}; T_0). \quad (35)$$

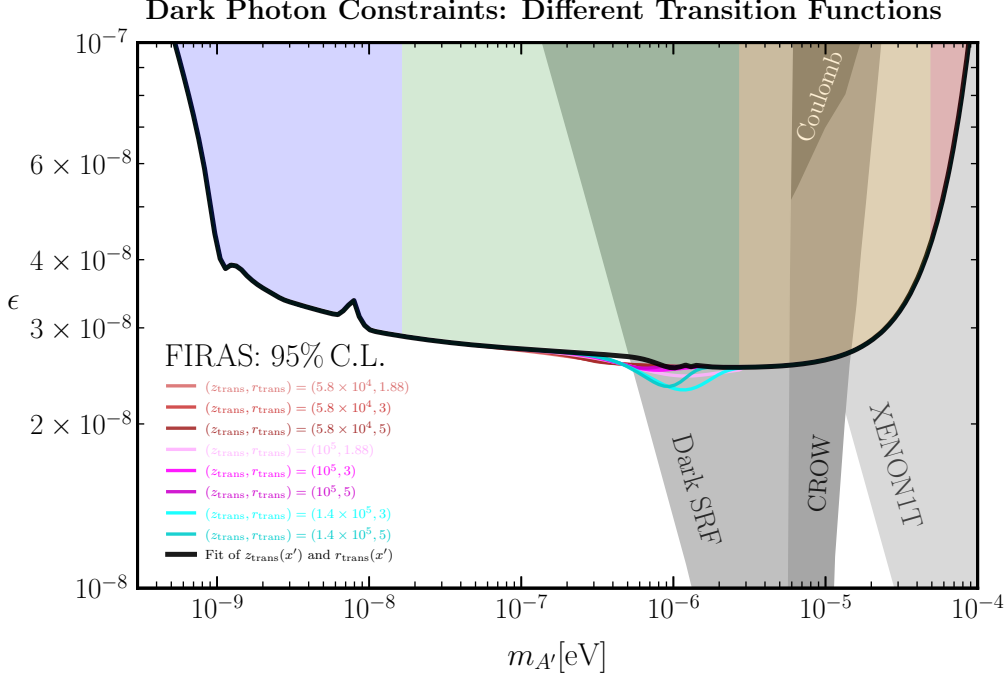


FIG. 7. The dark photon COBE-FIRAS constraint given different transition functions. As shown in Eq. (26), the transition function \mathcal{T}_μ is parameterized by two parameters z_{trans} and r_{trans} , which represent at which redshift and how fast the μ - y transition happens during the cosmological evolution. The black thick solid line is our fiducial constraint with $z_{\text{trans}}(x')$ and $r_{\text{trans}}(x')$ obtained by the fitting procedure described in the text. We can find that the dark photon COBE-FIRAS constraints with different z_{trans} and r_{trans} overlap in the dark photon mass range related to the whole free-streaming era, y -era, μ -era, T era, and most of the μ - y transition era. For the small portion of the $m_{A'}$ region where the COBE-FIRAS constraints with different parameterizations do not overlap, we draw this part of the constraint with the dashed line, which is the most conservative constraint among all the parameterizations of \mathcal{T}_μ .

Because the point “B” is at the side nearer to the y -era, the spectral distortion tends to be more like Eq. (30), which is close to the CMB spectral distortion under the free-streaming assumption (dashed black). Our approximation for $\Delta I_\gamma^{\text{trans}}$ in Eq. (35) depends on our choice of the parametrization of the transition function \mathcal{T}_μ inside G_{trans} .

Fig. 7 shows the different limits that we obtain under the different choices for the form of \mathcal{T}_μ discussed in Sec. IV. Our fiducial choice with z_{trans} and r_{trans} varying over x' is shown in black, while other choices of constant z_{trans} and r_{trans} are shown by the colored lines. We find that choosing different parametrizations of \mathcal{T}_μ leads to similar limits in the range $2 \times 10^{-8} \text{ eV} \lesssim m_{A'} \lesssim 2 \times 10^{-7} \text{ eV}$ in the μ - y transition region, where we therefore expect our limits to be robust. In this regime, the $\gamma \rightarrow A'$ transitions occur during a period when $G_{\text{trans}} \simeq G_y$, in agreement with the results shown in Ref. [67], and so the different parametrization choices are not important. We therefore label the limit that we obtain as a solid green line in Fig. 4 and subsequent figures. In the region $3 \times 10^{-7} \text{ eV} \lesssim m_{A'} \lesssim 3 \times 10^{-6} \text{ eV}$, we instead find differences in the limit on the order of a few tens of percent between different assumptions on z_{trans} and r_{trans} . However, the fiducial approach that we adopt also gives the weakest constraints in this range, and so we adopt the fiducial result as our limit. We denote our limit in Fig. 4 and subsequent figures with a dotted line, as an indication of the fact that our result may shift by a few tens of percent in ϵ . A more comprehensive, numerical approach in this limited mass range is still highly desirable, particularly for predicting the exact spectral shapes of distortions during this epoch.

As a closing remark, we want to stress that characterizing the CMB spectral distortion accurately can help us distinguish between different particle physics models. Consider, for example, the signals induced by the resonant $\gamma \rightarrow A'$ and $\gamma \rightarrow a$ transitions during the μ -era, where a denotes the axion-like particle. As discussed above, $\gamma \rightarrow A'$ induces a positive chemical potential shift. On the other hand, the resonant $\gamma \rightarrow a$ transition induces a negative

chemical potential shift instead. This is because the transition probability from CMB photon to axion satisfies $P_{\gamma \rightarrow a} \propto x'$ when $\gamma \rightarrow A'$ transition happens in the RAD universe [40]. Doing a similar analysis as above, we have $\mu_{\gamma \rightarrow a} \propto -(\langle x'^2 \rangle - x_0 \langle x' \rangle) < 0$, which has a sign difference compared to the dark photon in Eq. (34). The spectral distortion is therefore highly model dependent, and, when accurately determined, can give us information about the cause of any detected spectral distortion in the future.

VI. CONCLUSIONS

In this work, we have employed the Green's function method for photon injection and removal to perform an accurate determination of the COBE-FIRAS constraint on ϵ as a function of $m_{A'}$, due to spectral distortions arising from resonant $\gamma \rightarrow A'$ oscillations. Our updated limit transitions seamlessly to the free-streaming era constraint when $m_{A'} \lesssim 10^{-10}$ eV and maintains consistency and smoothness during the μ - y transition era. This contrasts with previous approaches which relied on inaccurate approximations, and did not tackle the problem self-consistently throughout the whole mass range of interest. Moreover, our methodology accurately predicts the shapes of CMB spectral distortions across different eras, which differ significantly from the predictions in previous work. This is crucial for identifying definitive signatures of $\gamma \rightarrow A'$ conversions in upcoming experiments aiming to measure CMB spectral distortions. Our limits from COBE-FIRAS, and future projections for next generation experiments such as PIXIE, form accurate benchmarks for experiments like DarkSRF, which are targeting dark photons in a similar mass range.

Note added. The results from this work were first presented by one of us in their PhD thesis [69] and at TeVPA 2024. While we were finalizing this submission, Ref. [106] appeared online, which also studies DP induced spectral distortions. Ref. [106] contains a full numerical treatment for spectral distortions, using the private code CosmoTherm [97], by one of the authors. A fully numerical approach allows the authors to treat also the regime of large spectral distortions, where the Green's function method that we use breaks down. However, this is only important for $m_{A'} \gtrsim 10^{-4}$ eV and kinetic mixing above $\sim 10^{-6}$. This region of the parameter space is already robustly excluded by other experiments, such as Xenon1T and solar emission constraints. For all parts of parameter space where our CMB spectral distortion limits are the most stringent constraint, distortions remain small, and the comparison between our results and those of Ref. [97] shows excellent agreement between our Green's function method and the full numerical treatment. All of our code and data are made public, including the fits for the Green's functions in the $\mu - y$ transition era which were not available before. These may also be applied in other contexts where photon injection or subtraction takes different forms.

VII. ACKNOWLEDGMENTS

We want to thank Jens Chluba, David Dunsky, Patrick J. Fox, Junwu Huang, Gustavo Marques-Tavares, and Clayton Ristow for helpful discussions. HL was supported by the Kavli Institute for Cosmological Physics and the University of Chicago through an endowment from the Kavli Foundation and its founder Fred Kavli, and Fermilab operated by the Fermi Research Alliance, LLC under contract DE-AC02-07CH11359 with the U.S. Department of Energy, Office of Science, Office of High-Energy Physics. XG and GA are supported by the James Arthur Graduate Associate (JAGA) Fellowship. The work of XG is supported in part by the Deutsche Forschungsgemeinschaft under Germany's Excellence Strategy - EXC 2121 "Quantum Universe" - 390833306. JTR is supported by NSF grant PHY-2210498. This work was performed in part at the Aspen Center for Physics, which is supported by NSF grant PHY-1607611. This research was supported in part by grant NSF PHY-2309135 to the Kavli Institute for Theoretical Physics (KITP). The work presented in this paper was performed on computational resources managed and supported by Princeton Research Computing. This work was supported in part through the NYU IT High Performance Computing resources, services, and staff expertise.

Appendix A: Profile Likelihood Test

The analysis of the COBE-FIRAS data in our paper follows Refs. [43, 44]. In this section, we give an introduction for completeness. To impose the constraint or the future projection on the dark photon's $\gamma \rightarrow A'$ oscillation using the data of the CMB spectral distortion, we use the constructed Gaussian likelihood function⁸

$$\log \mathcal{L}(\text{data}|m_{A'}, \epsilon) = \max_{T_0} \left\{ -\frac{1}{2} \delta \mathbf{I}_\gamma^T(m_{A'}, \epsilon; T_0) \cdot \mathbf{C}^{-1} \cdot \delta \mathbf{I}_\gamma(m_{A'}, \epsilon; T_0) \right\}. \quad (\text{A1})$$

\mathbf{C} is the $N_{\text{data}} \times N_{\text{data}}$ covariance matrix. N_{data} is the number of the data points. $\delta \mathbf{I}_\gamma(m_{A'}, \epsilon; T_0)$ is the N_{data} vector which is written as

$$\delta \mathbf{I}_\gamma(m_{A'}, \epsilon; T_0) = \bar{\mathbf{I}}_\gamma(T_0) + \Delta \mathbf{I}_\gamma(m_{A'}, \epsilon; T_0) - \bar{\mathbf{I}}_\gamma(T_{\text{data},0}) - \mathbf{R}, \quad (\text{A2})$$

where $T_{\text{data},0} = 2.7255\text{K}$ is the measured CMB temperature, \mathbf{R} is the N_{data} vector of residuals, and $\Delta \mathbf{I}_\gamma(m_{A'}, \epsilon; T_0)$ is the the $\gamma \rightarrow A'$ -induced CMB spectral distortion for all the frequency bins given the dark photon parameter $m_{A'}$ and ϵ . Note that $\bar{\mathbf{I}}_\gamma(T_{\text{data},0}) + \mathbf{R}$ is the observed COBE-FIRAS spectrum, and $\bar{\mathbf{I}}_\gamma(T_0) + \Delta \mathbf{I}_\gamma(m_{A'}, \epsilon; T_0)$ is the predicted CMB spectrum with distortions from dark photons with a blackbody temperature of T_0 , so that $\delta \mathbf{I}_\gamma$ is the difference between predicted and measured spectra. In the COBE-FIRAS dataset [49], $N_{\text{data}} = 43$ and the covariance matrix elements are

$$\mathcal{C}_{ij} = \sigma_i \sigma_j \mathcal{Q}_{|i-j|}, \quad (\text{A3})$$

where $i, j = 1, \dots, N_{\text{data}}$. Here, σ is the uncertainty and \mathcal{Q} is the $N_{\text{data}} \times 1$ vector which is

$$\mathcal{Q} = (\mathcal{Q}_0, \mathcal{Q}_1, \dots, \mathcal{Q}_{N_{\text{data}}-1}) = (1, 0.176, \dots, 0.008). \quad (\text{A4})$$

The test statistic is

$$\text{TS}(m_{A'}, \epsilon) = 2 \left[\log \mathcal{L}(\text{data}|m_{A'}, \epsilon) - \max_{\epsilon} \log \mathcal{L}(\text{data}|m_{A'}, \epsilon) \right], \quad (\text{A5})$$

which by Wilks' theorem [107, 108] follows a χ^2 -distribution with one degree of freedom. Therefore, to test A' with 95% confidence interval with a one-sided χ^2 distribution, we choose $\text{TS} = -2.71$ to impose the constraint on ϵ given $m_{A'}$.

Appendix B: Constants

In this section, we list the constants appearing in the calculation of the CMB spectral distortion and introduce their physical meanings. Firstly, we write down the following integrals

$$\begin{cases} \mathbb{T}_k = \int_0^\infty dx x^k \cdot \bar{f}_\gamma(x) \cdot \mathcal{T}(x) = (k+1)! \zeta(k+1), \\ \mathbb{F}_k = \int_0^\infty dx x^k \cdot \bar{f}_\gamma(x) = k! \zeta(k+1), \end{cases} \quad (\text{B1})$$

⁸ Since we are profiling over T_0 , when calculating the CMB spectral distortion happening in the μ -era, we only need to include the \mathbf{M} -term in Eq. (22) when utilizing Green's function method. This gives numerically more reliable results.

that are used in this paper. Given the fundamental ingredients shown in Eq. (B1), we can write all the constants appearing in the calculation of the CMB spectral distortion as

$$\alpha_\rho = \frac{\mathbb{F}_2}{\mathbb{F}_3} \simeq 0.3702, \quad \alpha_\mu = \frac{\mathbb{T}_1}{\mathbb{T}_2} \simeq 0.456, \quad x_0 = \frac{\mathbb{T}_3}{\mathbb{T}_2} = \frac{4}{3\alpha_\rho} \simeq 3.6, \quad \kappa_c = \frac{\mathbb{T}_1\mathbb{T}_3 - \mathbb{T}_2^2}{\mathbb{F}_2\mathbb{F}_3} \simeq 2.14185. \quad (\text{B2})$$

Here, α_ρ quantifies the ratio between $\bar{\rho}_\gamma$ and \bar{n}_γ , which is represented as

$$\alpha_\rho = \frac{\bar{n}_\gamma(T) T}{\bar{\rho}_\gamma(T)}. \quad (\text{B3})$$

α_μ quantifies the relation between the non-zero chemical potential and the temperature shift for the pure energy injection ($P_s = 0$) during the μ -era. In this case, the CMB photon's number density does not change. From Eq. (13) and Eq. (14), we have

$$P_s = 0: \quad \frac{t}{\mu} = \frac{\int d^3\mathbf{k} \bar{f}_\gamma(x) \cdot \mathcal{T}(x)/x}{\int d^3\mathbf{k} \bar{f}_\gamma(x) \cdot \mathcal{T}(x)} = \alpha_\mu. \quad (\text{B4})$$

x_0 is the dimensionless critical frequency for the photon injection or removal process. Let us take the monochromatic photon injection with the dimensionless frequency x as an example. For the low-frequency photon satisfying $x < P_s \cdot x_0$, the chemical potential from the photon injection flips sign compared with the pure energy injection. κ_c comes from solving the equations of the number density and energy density variations of the CMB photon caused by the photon injection. $3/\kappa_c \simeq 1.401$ is the numerical factor that frequently appears in former literature, such as Refs. [67, 98, 99, 109, 110], when describing the non-zero chemical potential developed during the μ -era.

Appendix C: Monochromatic Photon Injection in the μ -Era

In this section, we derive the chemical potential and temperature shift in the μ -era. As a simplified example, in this section, we only consider the monochromatic photon injection with frequency x_{inj} at the redshift z_{inj} , which gives

$$\Gamma_{\text{inj}}(x, z) = \tilde{\Gamma}_{\text{inj}} \delta(x - x_{\text{inj}}) \delta(z - z_{\text{inj}}). \quad (\text{C1})$$

In Appendix D3, we will give the Green's function formalism for the photon injection with the continuous spectrum and redshift in the μ -era.

From Eq. (13), we know that the variations in number density and energy density in the μ -era are

$$\begin{cases} P_s(x_{\text{inj}}, z_{\text{inj}}) \Delta n_{\gamma, \text{inj}} = g_\gamma \int d^3\mathbf{k} \Delta f_\gamma = \bar{n}_\gamma(T_{\text{inj}}) \left(\frac{\mathbb{T}_2}{\mathbb{F}_2} t_{\text{inj}} - \frac{\mathbb{T}_1}{\mathbb{F}_2} \mu_{\text{inj}} + \dots \right), \\ \Delta \rho_{\gamma, \text{inj}} = g_\gamma \int d^3\mathbf{k} \omega \Delta f_\gamma = \bar{\rho}_\gamma(T_{\text{inj}}) \left(\frac{\mathbb{T}_3}{\mathbb{F}_3} t_{\text{inj}} - \frac{\mathbb{T}_2}{\mathbb{F}_3} \mu_{\text{inj}} + \dots \right), \end{cases} \quad (\text{C2})$$

where μ_{inj} and t_{inj} represent the chemical potential and the temperature shift right of the CMB photon right after the happening of the photon injection. $\Delta n_{\gamma, \text{inj}}$ and $\Delta \rho_{\gamma, \text{inj}}$ represent the number density and energy density of injected photons, which are written as

$$\Delta n_{\gamma, \text{inj}} = \frac{d\bar{n}_\gamma}{dx_{\text{inj}}} \frac{\tilde{\Gamma}_{\text{inj}}}{(1 + z_{\text{inj}})H(z_{\text{inj}})} \quad \text{and} \quad \Delta \rho_{\gamma, \text{inj}} = x_{\text{inj}} T \Delta n_{\gamma, \text{inj}}. \quad (\text{C3})$$

P_s is the photon survival probability, quantifying the ratio of remaining injected photons after the photon absorption by DCS and BR. Solving Eq. (C2) and utilizing Eq. (B3), we have

$$\mu_{\text{inj}} = \alpha_\rho x_{\text{inj}} \cdot \frac{3}{\kappa_c} \left[1 - P_s(x_{\text{inj}}, z_{\text{inj}}) \frac{x_0}{x_{\text{inj}}} \right] \frac{\Delta n_{\gamma, \text{inj}}}{\bar{n}_\gamma}, \quad (\text{C4})$$

and

$$t_{\text{inj}} - \alpha_\mu \mu_{\text{inj}} = \alpha_\rho x_{\text{inj}} \cdot \frac{P_s}{4} \frac{x_0}{x_{\text{inj}}} \frac{\Delta n_{\gamma, \text{inj}}}{\bar{n}_\gamma}. \quad (\text{C5})$$

Because DCS and BR tend to drive the CMB photon's chemical potential to zero, today's CMB photon chemical potential μ_0 is μ_{inj} multiplied by the visibility function

$$\mathcal{J}^*(z) \simeq 0.983 \exp \left[- \left(\frac{z}{z_\mu} \right)^{2.5} \right] \left[1 - 0.0381 \left(\frac{z}{z_\mu} \right)^{2.29} \right], \quad \text{where } z_\mu \simeq 2 \times 10^6. \quad (\text{C6})$$

The derivation of Eq. (C6) can be found in [111]. Therefore, we have

$$\mu_0 = \alpha_\rho x_{\text{inj}} \cdot \frac{3}{\kappa_c} \mathcal{J}^*(z_{\text{inj}}) \left[1 - P_s(x_{\text{inj}}, z_{\text{inj}}) \frac{x_0}{x_{\text{inj}}} \right] \frac{\Delta n_{\gamma, \text{inj}}}{\bar{n}_\gamma}. \quad (\text{C7})$$

When $z_{\text{inj}} \gg z_\mu$, $\mathcal{J}^* \simeq 0$, therefore $\mu_0 \simeq 0$. When $z_{\text{inj}} \ll z_\mu$, $\mathcal{J}^* \simeq 1$, therefore $\mu_0 \simeq \mu_{\text{inj}}$. To illustrate the difference between the pure photon injection ($P_s \simeq 1$) and the pure energy injection ($P_s \simeq 0$), we compare the ratio of the CMB photon's chemical potentials in both cases and have

$$\frac{\mu_0|_{P_s=1}}{\mu_0|_{P_s=0}} \simeq 1 - \frac{x_0}{x_{\text{inj}}}. \quad (\text{C8})$$

From this equation, we find that when $x_{\text{inj}} < x_0$, the two chemical potentials have different signs. Therefore, for the photon injection in this frequency range, one cannot naively use the pure energy injection formalism in Ref. [99]. Otherwise, an extra minus sign may appear in the future signal of the CMB spectral distortion, which leads to the flipped signal.

For the generic photon injection/removal processes happening at the μ -era, the μ distortion can be decomposed into the linear superposition of the series of the monochromatic photon injection/removal processes. In this case, by doing the replacement $x_{\text{inj}} \rightarrow x'$, $z_{\text{inj}} \rightarrow z'$, $\tilde{\Gamma}_{\text{inj}} \rightarrow \Gamma_{\text{inj}}(x', z')$, the induced chemical potential shift can be written as

$$\mu = \int dz' \int dx' \alpha_\rho x' \left[1 - P_s(x', z') \frac{x_0}{x'} \right] \frac{d\bar{n}_\gamma/dx'}{\bar{n}_\gamma} \frac{\Gamma_{\text{inj}}(x', z')}{(1+z')H(z')}. \quad (\text{C9})$$

The above calculation is actually the derivation of the front factor of the first term in Eq. (22) which contains \mathbf{M} . The second term in Eq. (22) containing \mathbf{T} is derived utilizing the normalization condition listed in Eq. (21), which is equivalent to the energy conservation for the photon injection/removal processes.

Appendix D: Green's Functions

In this section, we introduce the calculation of the CMB spectral distortion utilizing Green's function method and list the concrete forms of Green's functions used in our work. Here, the CMB spectral distortion is

$$\Delta I_\gamma(x; T_0) = \int dx' \int dz' G(x; x', z'; T_0) S(x', z'). \quad (\text{D1})$$

$S(x', z')$ is the source of the photon injection, and it is written as⁹

$$S(x', z') = \frac{1}{\bar{n}_\gamma} \frac{d\bar{n}_\gamma}{dx'} \frac{\Gamma_{\text{inj}}(z')}{(1+z')H(z')}. \quad (\text{D2})$$

⁹ To get the source term in Ref. [67], we can do the replacement $S(x', z') \rightarrow 2\pi T_0 x' \cdot S(x', z')$.

Positive and negative Γ_{inj} represent the rate of the photon injection and removal, respectively¹⁰.

1. Functions

In this subsection, we summarize the functions that appear in appearing in Green's functions and are distributed throughout the main text. For the CMB photon whose phase space is exactly the black body, the intensity is

$$\bar{I}_\gamma(\omega_0; T_0) = \frac{\omega_0^3}{2\pi^2} \bar{f}_\gamma(x; T_0) = \frac{T_0^3}{2\pi^2} \frac{x^3}{e^x - 1}. \quad (\text{D3})$$

To describe the shape of the CMB spectral distortion, we have the dimensionless functions

$$\mathcal{T}(x) = \frac{x e^x}{e^x - 1}, \quad \mathcal{M}(x) = \mathcal{T}(x) \left(\alpha_\mu - \frac{1}{x} \right), \quad \mathcal{Y}(x) = \mathcal{T}(x) \left(x \frac{e^x + 1}{e^x - 1} - 4 \right), \quad (\text{D4})$$

where $\mathcal{T}(x)$ comes from the temperature shift, $\mathcal{M}(x)$ comes from the non-zero chemical potential, and $\mathcal{Y}(x)$ comes from the SZ effect. To describe the absolute CMB spectral distortion in terms of intensity, we define the functions

$$\begin{pmatrix} \mathbf{T}(x; T_0) \\ \mathbf{M}(x; T_0) \\ \mathbf{Y}(x; T_0) \end{pmatrix} = \bar{I}_\gamma(x; T_0) \times \begin{pmatrix} \mathcal{T}(x) \\ \mathcal{M}(x) \\ \mathcal{Y}(x) \end{pmatrix}, \quad (\text{D5})$$

which has the same dimension as the CMB intensity and the Green's functions. In this paper, we use Eq. (D4) and Eq. (D5) interchangeably depending on the convenience.

2. Green's Function Normalization

We now derive the Green's function normalization shown in Eq. (21). First, the relation between the distortion to the intensity of the CMB $\Delta I_\nu(x)$ and the total energy density of the distortion $\Delta \rho_\gamma$ is

$$\Delta \rho_\gamma = 2T_0 \int dx \Delta I_\gamma(x) = 2T_0 \int dx \int dx' \int dz' G(x; x', z'; T_0) S(x', z'), \quad (\text{D6})$$

where we have used the relation $xT_0 = 2\pi\nu_0$. On the other hand, from the Eq. (D2), we see that the injected energy density in the frequency interval between x' and $x' + dx'$, between redshifts z' and $z' + dz'$, is $x'T_0(1+z') \cdot \bar{n}_\gamma(T_0)(1+z')^3 \cdot S(x', z')$. This energy density redshifts as $(1+z)^4$; we therefore see that

$$\Delta \rho_\gamma = \int dx' \int dz' x' T_0 \bar{n}_\gamma(T_0) S(x', z'). \quad (\text{D7})$$

Comparing Eq. (D6) and Eq. (D7), we find

$$2T_0 \int dx G(x; x', z'; T_0) = x'T_0 \bar{n}_\gamma(T_0) = x' \alpha_\rho \bar{\rho}_\gamma(T_0), \quad (\text{D8})$$

where α_ρ is defined in Eq. (B3). Known as the normalization condition of Green's function, this equation is the same expression shown in Eq. (21).

¹⁰ For $\gamma \rightarrow A'$ resonant conversion, by substituting Eq. (3) into Eq. (D2), we can derive Eq. (19) under the narrow width approximation.

3. Green's Function in the μ -Era

For the CMB spectral distortion in the μ -era, we have

$$G_\mu(x; x', z'; T_0) = \alpha_\rho x' \cdot \frac{3}{\kappa_c} \mathcal{J}^*(z') \left[1 - P_s(x', z') \frac{x_0}{x'} \right] \mathbf{M}(x; T_0) + \frac{\lambda(x', z')}{4} \mathbf{T}(x; T_0), \quad (\text{D9})$$

where

$$\lambda(x', z') = \alpha_\rho x' \cdot \left[1 - \left(1 - P_s(x', z') \frac{x_0}{x'} \right) \mathcal{J}^*(z') \right]. \quad (\text{D10})$$

$P_s(x', z')$ is the survival probability function of the injected photons. During the μ -era, it can be approximately written as

$$P_s(x', z') = e^{-\tau_{\text{ff}}(x', z')}, \quad (\text{D11})$$

where $\tau_{\text{ff}}(x', z') \simeq x_c(z')/x'$. $\tau_{\text{ff}}(x', z')$ is the optical depth describing the absorption of the injected photons caused by BR and DCS, and $x_c(z')$ is the critical frequency for CS to dominate over BR and DCS. This is the pure energy injection. $\lambda(x', z')$ is determined by the normalization condition Eq. (21).

In our work, because we utilize the COBE-FIRAS data to explore $\gamma \rightarrow A'$, the photon frequency satisfying $x' \gg x_c(z')$ has the dominant contribution in the integration to calculate the CMB spectral distortion. Therefore, we approximately have $P_s(x', z') \simeq 1$. This is the pure photon injection. For the injection of the low-frequency photons satisfying $x' < x_0$, the non-zero chemical potential of the CMB photons has an extra minus sign compared with the chemical potential calculated under the framework of the pure energy injection where $P_s = 0$.

4. Green's Function in the y -Era

Here, we introduce the Green's function in the y -Era, which is written as

$$G_y(x; x', z'; T_0) = \alpha_\rho x' \cdot \left(1 - P_s(x', z') \frac{e^{(\alpha(x', z') + \beta(x', z')) y_\gamma(z')}}{1 + x' y_\gamma(z')} \right) \frac{\mathbf{Y}(x; T_0)}{4} + \alpha_\rho x' \cdot \frac{\bar{\rho}_\gamma(T_0)}{2T_0} P_s(x', z') F(x; x', z'). \quad (\text{D12})$$

Here, α and β are defined as

$$\alpha(x', z') = \frac{3 - 2f(x')}{\sqrt{1 + x' y_\gamma(z')}}, \quad \beta(x', z') = \frac{1}{1 + x' y_\gamma(z') [1 - f(x')]}, \quad (\text{D13})$$

where

$$f(x') = e^{-x'} \left(1 + \frac{x'^2}{2} \right). \quad (\text{D14})$$

F is defined as

$$F(x; x', z') = \frac{e^{-\frac{1}{4\beta(x', z') y_\gamma(z')}} \{ \log[x(1/x' + y_\gamma(z'))] - \alpha(x', z') y_\gamma(z') \}^2}{x' \sqrt{4\pi} \beta(x', z') y_\gamma(z')}. \quad (\text{D15})$$

Here, $F(x; x', z')$ obeys

$$\int_0^\infty dx F(x; x', z') = \frac{e^{(\alpha(x', z') + \beta(x', z')) y_\gamma(z')}}{1 + x' y_\gamma(z')}, \quad (\text{D16})$$

which helps us to easily check that Eq. (D12) satisfies the normalization condition in Eq. (21).

In the late universe such as the free-streaming era, y -era, or the late stage of the μ - y transition era, there is $y_\gamma \ll 1$ because the CS is inefficient. In such a situation, because $\alpha, \beta \sim \mathcal{O}(1)$, we can approximately write the second term in Eq. (D12) as

$$y_\gamma \ll 1: \quad F(x; x', z') \simeq \delta(x - x'). \quad (\text{D17})$$

In this case, the Green's function in Eq. (D12) can be approximately written as

$$y_\gamma \ll 1: \quad G_y(x; x', z'; T_0) \simeq \alpha_\rho x' \cdot (1 - P_s(x', z')) \frac{\mathbf{Y}(x; T_0)}{4} + \alpha_\rho x' \cdot \frac{\bar{\rho}_\gamma(T_0)}{2T_0} P_s(x', z') \delta(x - x'). \quad (\text{D18})$$

In the earlier universe, $F(x; x', z')$ is broadened by CS. Through the numerical comparison, we find that as long as $x'y_\gamma, \alpha y_\gamma, \beta y_\gamma \lesssim 1$, $F(x; x', z')$ can be well approximated by the Gaussian function $\frac{e^{(\alpha+\beta)y_\gamma}}{1+x'y_\gamma} \frac{e^{-(x-x_{\text{peak}})^2/\sigma^2}}{\sqrt{\pi}\sigma}$ with the standard deviation σ and the peak location x_{peak} . Here, the front factor of the Gaussian-type function is acquired by imposing the same normalization as Eq. (D16). By matching the peak of the Gaussian-type function and Eq. (D15), we have

$$\sigma = \frac{e^{(\alpha+\beta)y_\gamma}}{1+x'y_\gamma} \sqrt{4\beta y_\gamma x'}, \quad x_{\text{peak}} = \frac{e^{\alpha y_\gamma}}{1+x'y_\gamma} x'. \quad (\text{D19})$$

From the above equation, we can find that the larger y_γ is (CS is more efficient), or the larger x' is (CMB frequency is larger), the wider the $F(x; x', z')$ distribution is. In addition, when αy_γ or $x'y_\gamma$ is larger than $\mathcal{O}(1)$, the peak of this distribution will have a significant deviation from $x = x'$.

For the exploration of $\gamma \rightarrow A'$ using COBE-FIRAS data, we have $\tau_{\text{ff}} \ll 1$ because only the frequency range $x' \gtrsim 0.1$ inside the integration is relevant. This leads to $P_s \simeq 1$, which reveals that the $\gamma \rightarrow A'$ process is the pure photon removal. In this case, compared with the free-streaming term, the y distortion term has the subdominant contribution to the CMB spectral distortion.

5. Green's Function for Pure Energy Injection

In this section, we build the connection between the formalism describing the photon injection and the one describing the pure injection. By choosing the $P_s \rightarrow 0$ limit, which is the case for the injected low-frequency photon all absorbed by the thermal bath, the photon injection Green's function developed in Ref. [67] becomes the pure energy injection Green's function developed in Ref. [99].

Because $G(x, x', z'; T_0)/\alpha_\rho x'$ is independent of x' when $P_s(x', z') = 0$, we can define the Green's function for the pure energy injection as

$$G^{\text{th}}(x; z'; T_0) = \left. \frac{G(x; x', z'; T_0)}{\alpha_\rho x'} \right|_{P_s=0}. \quad (\text{D20})$$

Therefore, we can write Eq. (D1) and Eq. (D2) as

$$\Delta I_\gamma(x; T_0) = \int dz' G^{\text{th}}(x; z'; T_0) \frac{d(Q/\bar{\rho}_\gamma)}{dz'}, \quad (\text{D21})$$

where the speed of the energy injection can be written as

$$\frac{d(Q/\bar{\rho}_\gamma)}{dz'} = \int dx' \omega' \frac{d\bar{n}_\gamma/dx'}{\bar{\rho}_\gamma} \frac{\Gamma_{\text{inj}}(x', z')}{(1+z')H(z')}. \quad (\text{D22})$$

Applying Eq. (D20), we can derive the Green's functions for the thermalized energy injection, which are written as

$$G_{\mu}^{\text{th}}(x; z'; T_0) = \frac{3}{\kappa_c} \mathcal{J}^*(z') \mathbf{M}(x; T_0) + \frac{1 - \mathcal{J}^*(z')}{4} \mathbf{T}(x; T_0) \quad (\text{D23})$$

for the μ distortion, and

$$G_y^{\text{th}}(x; z'; T_0) = \frac{1}{4} \mathbf{Y}(x; T_0). \quad (\text{D24})$$

for the y distortion. We can find that Eq. (D21), Eq. (D23), and Eq. (D24) are all consistent with the formulas shown in Ref. [99]. We can also easily verify that both Eq. (D23) and Eq. (D24) satisfy the normalization condition of the pure energy injection, which is

$$2T_0 \int dx G^{\text{th}}(x; z'; T_0) = \bar{\rho}_{\gamma}(T_0). \quad (\text{D25})$$

-
- [1] D. F. Bartlett, P. E. Goldhagen, and E. A. Phillips, “Experimental Test of Coulomb’s Law,” *Phys. Rev. D* **2**, 483–487 (1970).
- [2] E. R. Williams, J. E. Faller, and H. A. Hill, “New experimental test of Coulomb’s law: A Laboratory upper limit on the photon rest mass,” *Phys. Rev. Lett.* **26**, 721–724 (1971).
- [3] D. F. Bartlett and S. Loegl, “LIMITS ON AN ELECTROMAGNETIC FIFTH FORCE,” *Phys. Rev. Lett.* **61**, 2285–2287 (1988).
- [4] D. Kroff and P. C. Malta, “Constraining hidden photons via atomic force microscope measurements and the Plimpton-Lawton experiment,” *Phys. Rev. D* **102**, 095015 (2020), [arXiv:2008.02209 \[hep-ph\]](#).
- [5] M. Betz, F. Caspers, M. Gasior, M. Thumm, and S. W. Rieger, “First results of the CERN Resonant Weakly Interacting sub-eV Particle Search (CROWS),” *Phys. Rev. D* **88**, 075014 (2013), [arXiv:1310.8098 \[physics.ins-det\]](#).
- [6] Asher Berlin *et al.*, “Searches for New Particles, Dark Matter, and Gravitational Waves with SRF Cavities,” (2022), [arXiv:2203.12714 \[hep-ph\]](#).
- [7] M. Diaz Ortiz *et al.*, “Design of the ALPS II optical system,” *Phys. Dark Univ.* **35**, 100968 (2022), [arXiv:2009.14294 \[physics.optics\]](#).
- [8] Akira Miyazaki, Tor Lofnes, Fritz Caspers, Paolo Spagnolo, John Jelonnek, Tobias Ruess, Johannes L. Steinmann, and Manfred Thumm, “Millimeter-Wave WISP Search with Coherent Light-Shining-Through-a-Wall Toward the STAX Project,” *Annalen Phys.* **536**, 2200619 (2024), [arXiv:2212.01139 \[hep-ph\]](#).
- [9] Asher Berlin, Roni Harnik, and Ryan Janish, “Light Shining Through a Thin Wall: Evanescent Hidden Photon Detection,” (2023), [arXiv:2303.00014 \[hep-ph\]](#).
- [10] C. Antel *et al.*, “Feebly-interacting particles: FIPs 2022 Workshop Report,” *Eur. Phys. J. C* **83**, 1122 (2023), [arXiv:2305.01715 \[hep-ph\]](#).
- [11] Javier Redondo, “Helioscope Bounds on Hidden Sector Photons,” *JCAP* **07**, 008 (2008), [arXiv:0801.1527 \[hep-ph\]](#).
- [12] Matthias Schwarz, Ernst-Axel Knabbe, Axel Lindner, Javier Redondo, Andreas Ringwald, Magnus Schneide, Jaroslav Susol, and Günter Wiedemann, “Results from the Solar Hidden Photon Search (SHIPS),” *JCAP* **08**, 011 (2015), [arXiv:1502.04490 \[hep-ph\]](#).
- [13] Jonas Frerick, Felix Kahlhoefer, and Kai Schmidt-Hoberg, “A’ view of the sunrise: boosting helioscopes with angular information,” *JCAP* **03**, 001 (2023), [arXiv:2211.00022 \[hep-ph\]](#).
- [14] T. O’Shea, M. Giannotti, I. G. Irastorza, L. M. Plasencia, J. Redondo, J. Ruz, and J. K. Vogel, “Prospects on the Detection of Solar Dark Photons by the International Axion Observatory,” (2023), [arXiv:2312.10150 \[hep-ph\]](#).
- [15] Haipeng An, Maxim Pospelov, Josef Pradler, and Adam Ritz, “Direct Detection Constraints on Dark Photon Dark Matter,” *Phys. Lett. B* **747**, 331–338 (2015), [arXiv:1412.8378 \[hep-ph\]](#).
- [16] Haipeng An, Maxim Pospelov, Josef Pradler, and Adam Ritz, “New limits on dark photons from solar emission and keV scale dark matter,” *Phys. Rev. D* **102**, 115022 (2020), [arXiv:2006.13929 \[hep-ph\]](#).
- [17] Robert Lasenby and Ken Van Tilburg, “Dark photons in the solar basin,” *Phys. Rev. D* **104**, 023020 (2021), [arXiv:2008.08594 \[hep-ph\]](#).
- [18] E. Aprile *et al.* (XENON), “Emission of single and few electrons in XENON1T and limits on light dark matter,” *Phys.*

- Rev. D **106**, 022001 (2022), [arXiv:2112.12116 \[hep-ex\]](#).
- [19] Maxim Pospelov, Adam Ritz, and Mikhail B. Voloshin, “Bosonic super-WIMPs as keV-scale dark matter,” *Phys. Rev. D* **78**, 115012 (2008), [arXiv:0807.3279 \[hep-ph\]](#).
- [20] Javier Redondo and Marieke Postma, “Massive hidden photons as lukewarm dark matter,” *JCAP* **02**, 005 (2009), [arXiv:0811.0326 \[hep-ph\]](#).
- [21] Javier Redondo and Georg Raffelt, “Solar constraints on hidden photons re-visited,” *JCAP* **08**, 034 (2013), [arXiv:1305.2920 \[hep-ph\]](#).
- [22] Haipeng An, Maxim Pospelov, and Josef Pradler, “New stellar constraints on dark photons,” *Phys. Lett. B* **725**, 190–195 (2013), [arXiv:1302.3884 \[hep-ph\]](#).
- [23] Nuria Vinyoles, Aldo Serenelli, Francesco Villante, Sarbani Basu, Javier Redondo, and Jordi Isern, “New Axion and Hidden Photon Constraints from a Solar Data Global Fit,” in *11th Patras Workshop on Axions, WIMPs and WISPs* (2015) pp. 92–95.
- [24] Javier Redondo, “Atlas of solar hidden photon emission,” *JCAP* **07**, 024 (2015), [arXiv:1501.07292 \[hep-ph\]](#).
- [25] Edward Hardy and Robert Lasenby, “Stellar cooling bounds on new light particles: plasma mixing effects,” *JHEP* **02**, 033 (2017), [arXiv:1611.05852 \[hep-ph\]](#).
- [26] Shao-Ping Li and Xun-Jie Xu, “Production rates of dark photons and Z' in the Sun and stellar cooling bounds,” *JCAP* **09**, 009 (2023), [arXiv:2304.12907 \[hep-ph\]](#).
- [27] Vitor Cardoso, Óscar J. C. Dias, Gavin S. Hartnett, Matthew Middleton, Paolo Pani, and Jorge E. Santos, “Constraining the mass of dark photons and axion-like particles through black-hole superradiance,” *JCAP* **03**, 043 (2018), [arXiv:1801.01420 \[gr-qc\]](#).
- [28] Hooman Davoudiasl and Peter B Denton, “Ultralight Boson Dark Matter and Event Horizon Telescope Observations of M87*,” *Phys. Rev. Lett.* **123**, 021102 (2019), [arXiv:1904.09242 \[astro-ph.CO\]](#).
- [29] Caner Ünal, Fabio Pacucci, and Abraham Loeb, “Properties of ultralight bosons from heavy quasar spins via superradiance,” *JCAP* **05**, 007 (2021), [arXiv:2012.12790 \[hep-ph\]](#).
- [30] Nils Siemonsen, Cristina Mondino, Daniel Egana-Ugrinovic, Junwu Huang, Masha Baryakhtar, and William E. East, “Dark photon superradiance: Electrodynamics and multimessenger signals,” *Phys. Rev. D* **107**, 075025 (2023), [arXiv:2212.09772 \[astro-ph.HE\]](#).
- [31] Leverett Davis, Jr., Alfred S. Goldhaber, and Michael Martin Nieto, “Limit on the photon mass deduced from Pioneer-10 observations of Jupiter’s magnetic field,” *Phys. Rev. Lett.* **35**, 1402–1405 (1975).
- [32] Giacomo Marocco, “Dark photon limits from magnetic fields and astrophysical plasmas,” (2021), [arXiv:2110.02875 \[hep-ph\]](#).
- [33] Shi Yan, Lingfeng Li, and JiJi Fan, “Constraints on photon mass and dark photon from the Jovian magnetic field,” (2023), [arXiv:2312.06746 \[hep-ph\]](#).
- [34] Alfred S. Goldhaber and Michael Martin Nieto, “Terrestrial and extra-terrestrial limits on the photon mass,” *Rev. Mod. Phys.* **43**, 277–296 (1971).
- [35] E. Fischbach, H. Kloor, R. A. Langel, A. T. Y. Liu, and M. Peredo, “New geomagnetic limits on the photon mass and on long range forces coexisting with electromagnetism,” *Phys. Rev. Lett.* **73**, 514–517 (1994).
- [36] H. Kloor, E. Fischbach, C. Talmadge, and G. L. Greene, “Limits on new forces coexisting with electromagnetism,” *Phys. Rev. D* **49**, 2098–2113 (1994).
- [37] Andrea Caputo, Alexander J. Millar, Ciaran A. J. O’Hare, and Edoardo Vitagliano, “Dark photon limits: A handbook,” *Phys. Rev. D* **104**, 095029 (2021), [arXiv:2105.04565 \[hep-ph\]](#).
- [38] Bob Holdom, “Two U(1)’s and Epsilon Charge Shifts,” *Phys. Lett. B* **166**, 196–198 (1986).
- [39] Alessandro Mirizzi, Javier Redondo, and Gunter Sigl, “Microwave Background Constraints on Mixing of Photons with Hidden Photons,” *JCAP* **03**, 026 (2009), [arXiv:0901.0014 \[hep-ph\]](#).
- [40] Alessandro Mirizzi, Javier Redondo, and Gunter Sigl, “Constraining resonant photon-axion conversions in the Early Universe,” *JCAP* **08**, 001 (2009), [arXiv:0905.4865 \[hep-ph\]](#).
- [41] Kerstin E. Kunze and Miguel Á. Vázquez-Mozo, “Constraints on hidden photons from current and future observations of CMB spectral distortions,” *JCAP* **12**, 028 (2015), [arXiv:1507.02614 \[astro-ph.CO\]](#).
- [42] Samuel D. McDermott and Samuel J. Witte, “Cosmological evolution of light dark photon dark matter,” *Phys. Rev. D* **101**, 063030 (2020), [arXiv:1911.05086 \[hep-ph\]](#).
- [43] Andrea Caputo, Hongwan Liu, Siddharth Mishra-Sharma, and Joshua T. Ruderman, “Dark Photon Oscillations in Our Inhomogeneous Universe,” *Phys. Rev. Lett.* **125**, 221303 (2020), [arXiv:2002.05165 \[astro-ph.CO\]](#).
- [44] Andrea Caputo, Hongwan Liu, Siddharth Mishra-Sharma, and Joshua T. Ruderman, “Modeling Dark Photon Oscillations in Our Inhomogeneous Universe,” *Phys. Rev. D* **102**, 103533 (2020), [arXiv:2004.06733 \[astro-ph.CO\]](#).
- [45] Andres Aramburo Garcia, Kyrlylo Bondarenko, Sylvia Ploeckinger, Josef Pradler, and Anastasia Sokolenko, “Effective

- photon mass and (dark) photon conversion in the inhomogeneous Universe,” *JCAP* **10**, 011 (2020), [arXiv:2003.10465 \[astro-ph.CO\]](#).
- [46] Dalila Pirvu, Junwu Huang, and Matthew C. Johnson, “Patchy screening of the CMB from dark photons,” *JCAP* **01**, 019 (2024), [arXiv:2307.15124 \[hep-ph\]](#).
- [47] Andres Aramburo-Garcia, Kyrylo Bondarenko, Alexey Boyarsky, Pavlo Kashko, Josef Pradler, Anastasia Sokolenko, Roi Kugel, Matthieu Schaller, and Joop Schaye, “Dark photon constraints from CMB temperature anisotropies,” (2024), [arXiv:2405.05104 \[astro-ph.CO\]](#).
- [48] Fiona McCarthy, Dalila Pirvu, J. Colin Hill, Junwu Huang, Matthew C. Johnson, and Keir K. Rogers, “Dark photon limits from patchy dark screening of the cosmic microwave background,” (2024), [arXiv:2406.02546 \[hep-ph\]](#).
- [49] D. J. Fixsen, E. S. Cheng, J. M. Gales, John C. Mather, R. A. Shafer, and E. L. Wright, “The Cosmic Microwave Background spectrum from the full COBE FIRAS data set,” *Astrophys. J.* **473**, 576 (1996), [arXiv:astro-ph/9605054](#).
- [50] Alessandro Mirizzi, Georg G. Raffelt, and Pasquale D. Serpico, “Photon-axion conversion as a mechanism for supernova dimming: Limits from CMB spectral distortion,” *Phys. Rev. D* **72**, 023501 (2005), [arXiv:astro-ph/0506078](#).
- [51] Hiroyuki Tashiro, Joseph Silk, and David J. E. Marsh, “Constraints on primordial magnetic fields from CMB distortions in the axiverse,” *Phys. Rev. D* **88**, 125024 (2013), [arXiv:1308.0314 \[astro-ph.CO\]](#).
- [52] Damian Ejlli and Alexander D. Dolgov, “CMB constraints on mass and coupling constant of light pseudoscalar particles,” *Phys. Rev. D* **90**, 063514 (2014), [arXiv:1312.3558 \[hep-ph\]](#).
- [53] Suvodip Mukherjee, Rishi Khatri, and Benjamin D. Wandelt, “Polarized anisotropic spectral distortions of the CMB: Galactic and extragalactic constraints on photon-axion conversion,” *JCAP* **04**, 045 (2018), [arXiv:1801.09701 \[astro-ph.CO\]](#).
- [54] Yacine Ali-Haïmoud, “Testing dark matter interactions with CMB spectral distortions,” *Phys. Rev. D* **103**, 043541 (2021), [arXiv:2101.04070 \[astro-ph.CO\]](#).
- [55] J. Chluba *et al.*, “Spectral Distortions of the CMB as a Probe of Inflation, Recombination, Structure Formation and Particle Physics: Astro2020 Science White Paper,” *Bull. Am. Astron. Soc.* **51**, 184 (2019), [arXiv:1903.04218 \[astro-ph.CO\]](#).
- [56] Clarence Zener, “Nonadiabatic crossing of energy levels,” *Proc. Roy. Soc. Lond. A* **137**, 696–702 (1932).
- [57] Lev Davidovich Landau, “Zur Theorie der Energieübertragung. II,” *Z. Sowjetunion* **2**, 46–51 (1932).
- [58] Kyrylo Bondarenko, Josef Pradler, and Anastasia Sokolenko, “Constraining dark photons and their connection to 21 cm cosmology with CMB data,” *Phys. Lett. B* **805**, 135420 (2020), [arXiv:2002.08942 \[astro-ph.CO\]](#).
- [59] Paola Arias, Davide Cadamuro, Mark Goodsell, Joerg Jaeckel, Javier Redondo, and Andreas Ringwald, “WISPy Cold Dark Matter,” *JCAP* **06**, 013 (2012), [arXiv:1201.5902 \[hep-ph\]](#).
- [60] Sergei Dubovsky and Guzmán Hernández-Chifflet, “Heating up the Galaxy with Hidden Photons,” *JCAP* **12**, 054 (2015), [arXiv:1509.00039 \[hep-ph\]](#).
- [61] Digvijay Wadekar and Glennys R. Farrar, “Gas-rich dwarf galaxies as a new probe of dark matter interactions with ordinary matter,” *Phys. Rev. D* **103**, 123028 (2021), [arXiv:1903.12190 \[hep-ph\]](#).
- [62] Samuel J. Witte, Salvador Rosauro-Alcaraz, Samuel D. McDermott, and Vivian Poulin, “Dark photon dark matter in the presence of inhomogeneous structure,” *JHEP* **06**, 132 (2020), [arXiv:2003.13698 \[astro-ph.CO\]](#).
- [63] Haipeng An, Fa Peng Huang, Jia Liu, and Wei Xue, “Radio-frequency Dark Photon Dark Matter across the Sun,” *Phys. Rev. Lett.* **126**, 181102 (2021), [arXiv:2010.15836 \[hep-ph\]](#).
- [64] Haipeng An, Shuailiang Ge, Wen-Qing Guo, Xiaoyuan Huang, Jia Liu, and Zhiyao Lu, “Direct Detection of Dark Photon Dark Matter Using Radio Telescopes,” *Phys. Rev. Lett.* **130**, 181001 (2023), [arXiv:2207.05767 \[hep-ph\]](#).
- [65] Haipeng An, Shuailiang Ge, Jia Liu, and Mingzhe Liu, “In-situ Measurements of Dark Photon Dark Matter using Parker Solar Probe: Going beyond the Radio Window,” (2024), [arXiv:2405.12285 \[hep-ph\]](#).
- [66] Haipeng An, Shuailiang Ge, Jia Liu, and Zhiyao Lu, “Direct Detection of Dark Photon Dark Matter with the James Webb Space Telescope,” (2024), [arXiv:2402.17140 \[hep-ph\]](#).
- [67] Jens Chluba, “Green’s function of the cosmological thermalization problem – II. Effect of photon injection and constraints,” *Mon. Not. Roy. Astron. Soc.* **454**, 4182–4196 (2015), [arXiv:1506.06582 \[astro-ph.CO\]](#).
- [68] A. Romanenko *et al.*, “Search for Dark Photons with Superconducting Radio Frequency Cavities,” *Phys. Rev. Lett.* **130**, 261801 (2023), [arXiv:2301.11512 \[hep-ex\]](#).
- [69] Xucheng Gan, “The Hidden Universe Odyssey: From Theoretical Foundations to Cosmological Detections,” *PhD Thesis* (2024).
- [70] Xucheng Gan, “CMB spectral distortions from dark photon oscillation,” in *Proceedings of the 2024 TeV Particle Astrophysics Conference (TeVPA 2024)* (University of Chicago, 2024) conference presentation.
- [71] Steven Weinberg, *The quantum theory of fields. Vol. 2: Modern applications* (Cambridge University Press, 2013).
- [72] C. P. Burgess, J. P. Conlon, L-Y. Hung, C. H. Kom, Anshuman Maharana, and F. Quevedo, “Continuous Global

- Symmetries and Hyperweak Interactions in String Compactifications,” *JHEP* **07**, 073 (2008), [arXiv:0805.4037 \[hep-th\]](#).
- [73] Tony Gherghetta, Jörn Kersten, Keith Olive, and Maxim Pospelov, “Evaluating the price of tiny kinetic mixing,” *Phys. Rev. D* **100**, 095001 (2019), [arXiv:1909.00696 \[hep-ph\]](#).
- [74] Xucheng Gan and Di Liu, “Cosmologically varying kinetic mixing,” *JHEP* **11**, 031 (2023), [arXiv:2302.03056 \[hep-ph\]](#).
- [75] Xucheng Gan and Yu-Dai Tsai, “Cosmic Millicharge Background and Reheating Probes,” (2023), [arXiv:2308.07951 \[hep-ph\]](#).
- [76] Ella Iles, Saniya Heeba, and Katelin Schutz, “Direct Detection of the Millicharged Background,” (2024), [arXiv:2407.21096 \[hep-ph\]](#).
- [77] Asher Berlin, Jeff A. Dror, Xucheng Gan, and Joshua T. Ruderman, “Millicharged relics reveal massless dark photons,” *JHEP* **05**, 046 (2023), [arXiv:2211.05139 \[hep-ph\]](#).
- [78] Asher Berlin, Raffaele Tito D’Agnolo, Sebastian A. R. Ellis, and Jury I. Radkovski, “Signals of millicharged dark matter in light-shining-through-wall experiments,” *JHEP* **08**, 017 (2023), [arXiv:2305.05684 \[hep-ph\]](#).
- [79] Jae Hyeok Chang, David E. Kaplan, Surjeet Rajendran, Harikrishnan Ramani, and Erwin H. Tanin, “Dark Solar Wind,” *Phys. Rev. Lett.* **129**, 211101 (2022), [arXiv:2205.11527 \[hep-ph\]](#).
- [80] Damiano F. G. Fiorillo and Edoardo Vitagliano, “Self-interacting dark sectors in supernovae are fluid,” (2024), [arXiv:2404.07714 \[hep-ph\]](#).
- [81] Max Born and Emil Wolf, *Principles of optics* (Cambridge Univ. Pr., 1999).
- [82] Yacine Ali-Haïmoud and Christopher M. Hirata, “HyRec: A fast and highly accurate primordial hydrogen and helium recombination code,” *Phys. Rev. D* **83**, 043513 (2011), [arXiv:1011.3758 \[astro-ph.CO\]](#).
- [83] Nanoom Lee and Yacine Ali-Haïmoud, “HYREC-2: a highly accurate sub-millisecond recombination code,” *Phys. Rev. D* **102**, 083517 (2020), [arXiv:2007.14114 \[astro-ph.CO\]](#).
- [84] N. Aghanim *et al.* (Planck), “Planck 2018 results. VI. Cosmological parameters,” *Astron. Astrophys.* **641**, A6 (2020), [Erratum: *Astron. Astrophys.* 652, C4 (2021)], [arXiv:1807.06209 \[astro-ph.CO\]](#).
- [85] Stephen J. Parke, “Nonadiabatic Level Crossing in Resonant Neutrino Oscillations,” *Phys. Rev. Lett.* **57**, 1275–1278 (1986).
- [86] Tzee-Ke Kuo and James T. Pantaleone, “Neutrino Oscillations in Matter,” *Rev. Mod. Phys.* **61**, 937 (1989).
- [87] Nirmalya Brahma, Asher Berlin, and Katelin Schutz, “Photon-dark photon conversion with multiple level crossings,” *Phys. Rev. D* **108**, 095045 (2023), [arXiv:2308.08586 \[hep-ph\]](#).
- [88] A. F. Illarionov and R. A. Sunyaev, “Comptonization, the background-radiation spectrum, and the thermal history of the universe,” *sovast* **18**, 691–699 (1975).
- [89] K. L. Chan and B. J. T. Jones, “The evolution of the cosmic radiation spectrum under the influence of turbulent heating. I. Theory.” *Astrophys. J.* **200**, 454–470 (1975).
- [90] L. Danese and G. de Zotti, “On distortions in the Rayleigh-Jeans region of the cosmic background radiation spectrum,” *aap* **84**, 364 (1980).
- [91] L. Danese and G. de Zotti, “Double Compton process and the spectrum of the microwave background,” *aap* **107**, 39–42 (1982).
- [92] R. A. Sunyaev and Ya. B. Zeldovich, “The interaction of matter and radiation in the hot model of the Universe, II,” *apss* **7**, 20–30 (1970).
- [93] Ya. B. Zeldovich and R. A. Sunyaev, “The Interaction of Matter and Radiation in a Hot-Model Universe,” *apss* **4**, 301–316 (1969).
- [94] R. A. Daly, “Spectral Distortions of the Microwave Background Radiation Resulting from the Damping of Pressure Waves,” *Astrophys. J.* **371**, 14 (1991).
- [95] Wayne Hu and Joseph Silk, “Thermalization and spectral distortions of the cosmic background radiation,” *Phys. Rev. D* **48**, 485–502 (1993).
- [96] Wayne T. Hu, *Wandering in the Background: A CMB Explorer*, Other thesis (1995), [arXiv:astro-ph/9508126](#).
- [97] J. Chluba and R. A. Sunyaev, “The evolution of CMB spectral distortions in the early Universe,” *Mon. Not. Roy. Astron. Soc.* **419**, 1294–1314 (2012), [arXiv:1109.6552 \[astro-ph.CO\]](#).
- [98] Jens Chluba and Donghui Jeong, “Teasing bits of information out of the CMB energy spectrum,” *Mon. Not. Roy. Astron. Soc.* **438**, 2065–2082 (2014), [arXiv:1306.5751 \[astro-ph.CO\]](#).
- [99] Jens Chluba, “Green’s function of the cosmological thermalization problem,” *Mon. Not. Roy. Astron. Soc.* **434**, 352 (2013), [arXiv:1304.6120 \[astro-ph.CO\]](#).
- [100] Sandeep Kumar Acharya and Rishi Khatri, “Rich structure of non-thermal relativistic CMB spectral distortions from high energy particle cascades at redshifts $z \lesssim 2 \times 10^5$,” *Phys. Rev. D* **99**, 043520 (2019), [arXiv:1808.02897 \[astro-ph.CO\]](#).
- [101] A. Kogut *et al.*, “The Primordial Inflation Explorer (PIXIE): A Nulling Polarimeter for Cosmic Microwave Background Observations,” *JCAP* **07**, 025 (2011), [arXiv:1105.2044 \[astro-ph.CO\]](#).

- [102] Alan Kogut *et al.*, “The Primordial Inflation Explorer (PIXIE): Mission Design and Science Goals,” (2024), [arXiv:2405.20403 \[astro-ph.CO\]](#).
- [103] Jens Chluba, Andrea Ravenni, and Sandeep Kumar Acharya, “Thermalization of large energy release in the early Universe,” *Mon. Not. Roy. Astron. Soc.* **498**, 959–980 (2020), [arXiv:2005.11325 \[astro-ph.CO\]](#).
- [104] Julien Lesgourgues, “The Cosmic Linear Anisotropy Solving System (CLASS) I: Overview,” (2011), [arXiv:1104.2932 \[astro-ph.IM\]](#).
- [105] Diego Blas, Julien Lesgourgues, and Thomas Tram, “The Cosmic Linear Anisotropy Solving System (CLASS) II: Approximation schemes,” *JCAP* **07**, 034 (2011), [arXiv:1104.2933 \[astro-ph.CO\]](#).
- [106] Jens Chluba, Bryce Cyr, and Matthew C. Johnson, “Revisiting Dark Photon Constraints from CMB Spectral Distortions,” (2024), [arXiv:2409.12115 \[astro-ph.CO\]](#).
- [107] S. S. Wilks, “The Large-Sample Distribution of the Likelihood Ratio for Testing Composite Hypotheses,” *Annals Math. Statist.* **9**, 60–62 (1938).
- [108] R. L. Workman *et al.* (Particle Data Group), “Review of Particle Physics,” *PTEP* **2022**, 083C01 (2022).
- [109] J. Chluba *et al.*, “New horizons in cosmology with spectral distortions of the cosmic microwave background,” *Exper. Astron.* **51**, 1515–1554 (2021), [arXiv:1909.01593 \[astro-ph.CO\]](#).
- [110] Anson Hook, Gustavo Marques-Tavares, and Clayton Ristow, “CMB spectral distortions from an axion-dark photon-photon interaction,” *JHEP* **05**, 086 (2024), [arXiv:2306.13135 \[hep-ph\]](#).
- [111] Jens Chluba, “Refined approximations for the distortion visibility function and μ -type spectral distortions,” *Mon. Not. Roy. Astron. Soc.* **440**, 2544–2563 (2014), [arXiv:1312.6030 \[astro-ph.CO\]](#).